International Journal of Plasticity 133 (2020) 102819

Contents lists available at ScienceDirect

International Journal of Plasticity

journal homepage: http://www.elsevier.com/locate/ijplas

Unraveling the dislocation–precipitate interactions in high-entropy alloys

Jia Li [a], Haotian Chen [a], Qihong Fang [a,*], Chao Jiang [a,**], Yong Liu [b,***], Peter K. Liaw [c]

[a] State Key Laboratory of Advanced Design and Manufacturing for Vehicle Body, Hunan University, Changsha, 410082, PR China
[b] State Key Laboratory of Powder Metallurgy, Central South University, Changsha, 410083, PR China
[c] Department of Materials Science and Engineering, The University of Tennessee, Knoxville, TN, 37996, USA

ARTICLE INFO

Keywords:
High-entropy alloy
Coherent precipitate strengthening
Stacking fault strengthening
Atomic-scale lattice distortion
Cryogenic/elevated temperatures
Molecular dynamics

ABSTRACT

The precipitates play a significant role in not only enhancing the strength, but also maintaining the high toughness in alloys. However, the interactions of the nanoscale precipitates with dislocations in the high entropy alloys (HEAs) are difficult to observe directly by in-situ TEM experiments due to the limits of the resolution and time. Here, using atomic simulations we report the synergistic strengthening of the coherent precipitate and atomic-scale lattice distortion in the HEAs at cryogenic/elevated temperatures. The effects of temperature, chemical disorder, precipitate spacing, precipitate size, elemental segregation, and dislocation-cutting number on the critical stress for the dislocation to overcome a row of precipitates are studied. A random stacking fault energy landscape along the slip plane, the lattice distortion at different temperatures, and the interface/surface energy at various crystallographic orientations are obtained. Compared with the traditional metals and alloys, HEAs have the severe atomic-scale lattice distortions to generate the local high tensile/compressive stress fields. This complex stress causes the dislocation line to bend, and thus improves the dislocation slip resistance, resulting in the strong solid-solution strengthening. The stacking fault strengthening induced by the obvious difference of the stacking fault energies between the HEA matrix and precipitate (within the inner of the HEA matrix), and the formation of the antiphase domain boundary contribute to the high strength. The precipitate embedded by the solute atoms produces the strong lattice distortion to enhance the dislocation slip resistance at high temperatures. Hence, the current results provide the mechanistic insight into the phenomenon that the coherent precipitate combined with the severe atomic-scale lattice distortion can enhance the strength at cryogenic/elevated temperatures to further broaden the scope of applications of advanced HEAs.

1. Introduction

In order to meet the requirements for extreme environments, for example, cryogenic or elevated temperatures, the materials with

* Corresponding author.
** Corresponding author.
*** Corresponding author.
E-mail addresses: fangqh1327@hnu.edu.cn (Q. Fang), jiangc@hnu.edu.cn (C. Jiang), yonliu@csu.edu.cn (Y. Liu).

https://doi.org/10.1016/j.ijplas.2020.102819
Received 24 March 2020; Received in revised form 7 July 2020; Accepted 7 July 2020
Available online 20 July 2020

the high strength and high structural stability are necessary (Zhou et al., 2018; Chen et al., 2016; Feng et al., 2017; Ding et al., 2018a,b; Ding et al., 2019; Ming et al., 2019; Smith et al., 2016; Gludovatz et al., 2016; Yang et al., 2018a). However, the pure metals rarely have such excellent mechanical properties. Consequently, other material elements are added, in order to adjust the microstructures and improve the mechanical properties. The traditional single-element dominant alloys, such as Fe-based steels, Ti-based alloys, and Ni-based superalloys, are well studied to obtain their high strength and toughness. Recently, the multi-component alloys consisting of near-equiatomic five or more base metals are proposed, and named high-entropy alloys (HEAs), multiple element alloys (MEAs), multicomponent alloys (MA), multi-principal element alloys (MPEAs), complex concentrated alloys (CCAs), compositionally complex alloys (CCAs), baseless alloys (BAs), or metal buffets (MBs) (Yeh et al., 2004; Diao et al., 2017; Zhang et al., 2014; Gao et al., 2016).

These HEAs or MEAs show much better mechanical properties than the conventional alloys. It is reported that the effects of the severe lattice distortion, high entropy, sluggish diffusion, and cocktail play key roles in the deformation and strengthening mechanisms of the HEAs (Yeh et al., 2004; Diao et al., 2017; Zhang et al., 2014, 2018a; Gao et al., 2016; Wu et al., 2019; Miracle and Senkov, 2017; Varvenne et al., 2016; Rao et al., 2017a). For example, the CrMnFeCoNi HEA displays the excellent strength and toughness at cryogenic temperatures down to 77 K, which is attributed to a deformation transition from the planar-slip dislocation at room temperature to mechanical nanotwinning with the decreasing temperature (Gludovatz et al., 2014). Moreover, the HEAs exhibit the good yielding strength and high ductility at elevated temperatures (Zou et al., 2015; Huang et al., 2017; Jiang et al., 2017a), owing to the high thermal stability.

Moreover, to further improve the strengths of the HEAs, the precipitate-strengthened HEAs have been developed rapidly (He et al., 2016; Yao et al., 2018; Ming et al., 2018; Gwalani et al., 2016; Xu et al., 2015; Wang et al., 2016; Ma et al., 2017). The precipitates not only interact with dislocations, but also promote the formation of antiphase domain boundaries (APB) to enhance the strength (Zhang et al., 2018b; Zhao et al., 2018; Yang et al., 2018b; Liang et al., 2018; Fu et al., 2018). To deeply understand the mechanism of the precipitate-dislocation interactions, molecular dynamics (MD) simulations as an effective tool have been performed to study the precipitate strengthening and dislocation dynamic behavior in the pure metals and alloys (Bacon et al., 2009; Zhou et al., 2011; Antillon et al., 2019; Osetsky et al., 2019; Rao et al., 2017b). The work mentioned above has concentrated on the hard precipitate to enhance the yielding strength of the alloys (Zhang et al., 2018b; Zhao et al., 2018; Yang et al., 2018b; Santos-Güemes et al., 2018; Li and Huang, 2018; 2018). Unlike the hard precipitate, a soft and coherent precipitate in the steels not only improves the strength but also does not cause a decrease in the toughness (Ghosh et al., 2011). The conventional alloys produce the low lattice distortion, but the severe lattice distortion is generated in the HEAs and strongly affects the short-range interaction between the dislocation and precipitate (Yang et al., 2018b; Liang et al., 2018; Fu et al., 2018; Bacon et al., 2009). However, the detailed microstructural evolution of the coherent precipitate interacting with dislocations subjected to the severe atomic-level lattice distortion is relatively unknown, especially for the service at cryogenic/elevated temperatures in the HEAs.

The aim of this study is to gain the fundamental understanding of the coherent precipitate-strengthening effect in the HEAs at cryogenic or elevated temperatures. Based on atomic simulations, the interaction of the dislocation and coherent precipitate is revealed at cryogenic/elevated temperatures. The influences of the severe atomic-scale lattice distortion, temperature, chemical disorder, precipitate size, precipitate spacing, and dislocation-cutting number on the strengthening behavior are quantitatively investigated in detail. Furthermore, the mechanical properties of the HEA with the coherent precipitates are compared with the previous studies (Gludovatz et al., 2014; Zou et al., 2015; Jiang et al., 2017a), to uncover the precipitate-strengthening mechanism.

2. MD simulation details

2.1. Atomic modeling and potential

The shear deformation of the precipitate-strengthened HEA is investigated by MD simulations. All MD simulations are carried out, using the embedded atom method (EAM) potential developed in Ref. (Zhou et al., 2004). Recently, the EAM potentials have been widely applied to study the dislocation behaviour (Rao et al., 2017a, b; Nöhring and Curtin, 2017; Osetsky et al., 2019), grain boundary structure (Utt et al., 2020), and phase transformation (Li et al., 2018; Bahramyan et al., 2020) in the HEAs. The previous experiment shows that the nanocrystalline $Co_{25}Ni_{25}Fe_{25}Al_{7.5}Cu_{17.5}$ (atomic percent, at.%) HEA exhibits a much higher yield strength than the most face-centered-cubic (FCC) structured HEAs (Fu et al., 2016). Hence, the $Co_{25}Ni_{25}Fe_{25}Al_{7.5}Cu_{17.5}$ HEA is selected for the present study. Fig. 2 presents the variation of the cohesive energy per atom as a function of the lattice parameter for the FCC $Co_{25}Ni_{25}Fe_{25}Al_{7.5}Cu_{17.5}$ HEA, where the equilibrium lattice parameter of 3.603 Å agrees with the lattice constant obtained by the experiment (Fu et al., 2016). Here, the stacking-fault energy (SFE) of the $Co_{25}Ni_{25}Fe_{25}Al_{7.5}Cu_{17.5}$ HEA is exhibited in Fig. 3. This value of 5.10 mJ/m^2 is consistent with the previous reports of the non-equiatomic HEA having a low SFE, such as 6.31 mJ/m^2 in the Fe40Mn20Cr15Co20Si5 HEA (Frank et al., 2020), 3.5 mJ/m^2 in the Co20Cr26Fe20Mn20Ni14 HEA (Zaddach et al., 2013), and 8 mJ/m^2 in the Ni14Cr21.5Co21.5Fe21.5Mn21.5 HEA (Vikram et al., 2019). The energy of extrinsic stacking fault is 5.21 mJ/m^2 is also similar to the recent reports, such as 3 mJ/m^2 in the CrMnFeCoNi HEA (Sun et al., 2020), and 1 mJ/m^2 in the CrCoNiMn HEA (Huang et al., 2018a,b). The twin boundary energy of 5.11 mJ/m^2 is close to the recent result, such as 11 mJ/m^2 in the CrCoNi MEA (Zhang et al., 2017; Li et al., 2019), and 8 mJ/m^2 in the FeCrCoNiMn HEA (Huang et al., 2015, 2018a,b). Moreover, the current EAM potential could accurately predict the yielding strength of the $Co_{25}Ni_{25}Fe_{25}Al_{7.5}Cu_{17.5}$ HEA in our previous work (Li et al., 2018), in according with the previous experimental value (Fu et al., 2016). In order to reveal the influence of lattice distortion, the interaction between the precipitate and dislocation in the pure Ni is simulated and compared, and the EAM potential is also applied to this system (Onat and Durukanoğlu, 2013).

The shear-deformation model of the HEA consists of a HEA matrix and a coherent nanoscale precipitate using MD simulations, as

exhibited in Fig. 1(a and b). Here, the full edge dislocation can spontaneously split into two Shockley partials separated by a stacking fault (Fig. 1b), which is consistent with the dislocation structure reported in the HEAs (Rao et al., 2017a, b; Osetsky et al., 2019). This result further proves the correctness of the current EAM potential, to study the dislocation evolution and motion under the deformation. During MD simulations, the distributions of various elements are roughly uniform at the large sale and have the small peaks, so that some elemental segregations occur in the HEA (Fig. 4b and c). The atom types along the slip plane are different, where the like-element atoms should be separated from each other (Figs. 1c and 4b). This chemical configuration of atoms leads to the severe lattice distortion at atomic scale, due to the difference of atom radii (Table 1). The atomic number of the HEA matrix is about 1,270, 000, and the sample size is $40.8 \times 19.4 \times 18.7$ nm^3. The orientations of x, y, and z axes are along $[1\bar{1}0]$, $[11\bar{2}]$, and [1 1 1] directions, respectively (Bacon et al., 2009). The center of the spherical coherent precipitate with a radius of 3 nm is set on the dislocation-slip plane. The perfect edge dislocation is introduced on the <110> slip plane, and the distance between the particle surface and the

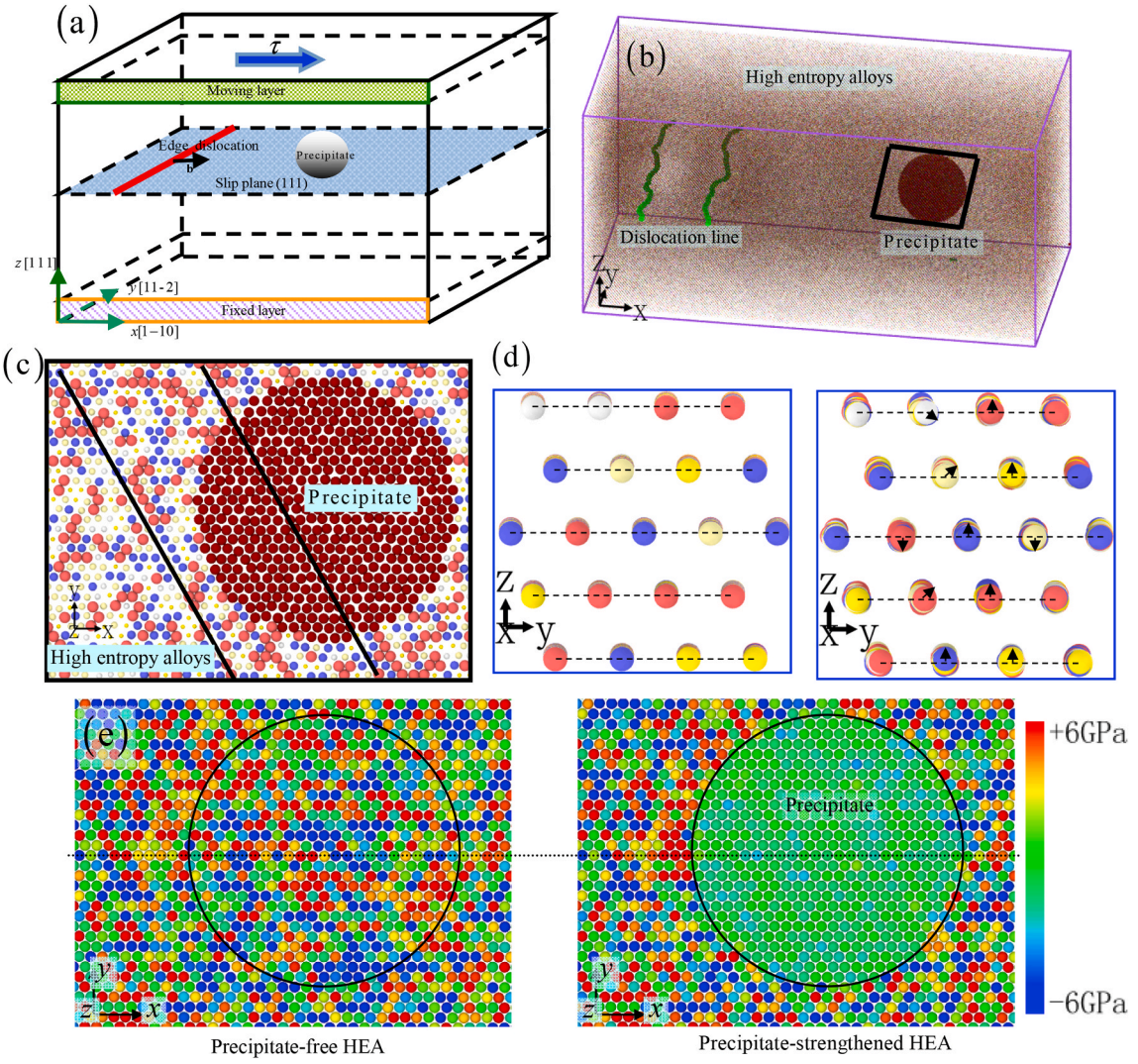

Fig. 1. (a) Schematic of a dislocation interacting with a coherent precipitate during the shear deformation. The edge dislocation moves towards the coherent precipitate under the shear loading. The shear deformation is generated to the crystal by moving the upper atom layers. (b) Atomic model of the dislocation-precipitate interaction in the $Co_{25}Ni_{25}Fe_{25}Al_{7.5}Cu_{17.5}$ HEA. Based on the atom type, Co, Ni, Fe, Al, and Cu. To highlight the precipitate, the corresponding atoms are colored by the dark red. The green lines stand for the partial dislocation lines. (c) Partially-enlarged view of the elemental distribution nearby the coherent precipitate, as shown in (b). (d) Atoms of the pristine structure occupying the ideal lattice positions, which subsequently stray from their ideal positions after lattice distortion. An arrow represents the general direction of the atomic deviation. Hence, the atoms deviate from the original position, resulting in the atomic-scale lattice distortion. (e) For the same position nearby the precipitate, the distribution of stress τ_{xz} on the dislocation-slip plane in the precipitate-free HEA, and in the precipitate-strengthened HEA, respectively. The red atoms indicate the high tensile stress region, the blue atoms denote the high compressive stress region, and the green atoms represent the low stress region or the stress-free region. The high stress on the left side of the precipitate is due to the elastic mismatch. (For interpretation of the references to color in this figure legend, the reader is referred to the Web version of this article.)

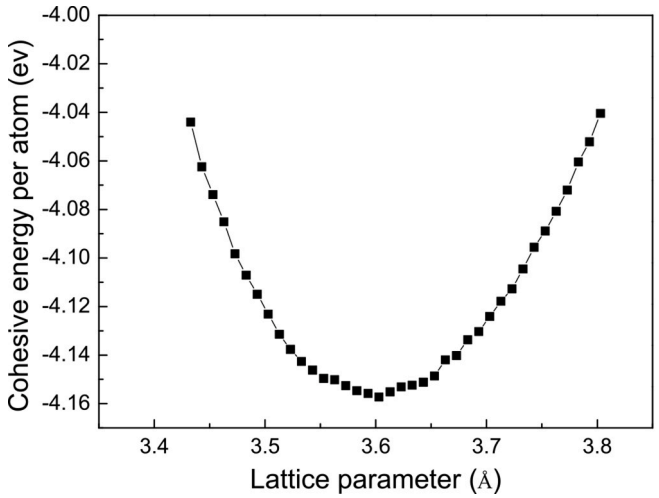

Fig. 2. Cohesive energy vs lattice parameter of the FCC HEA.

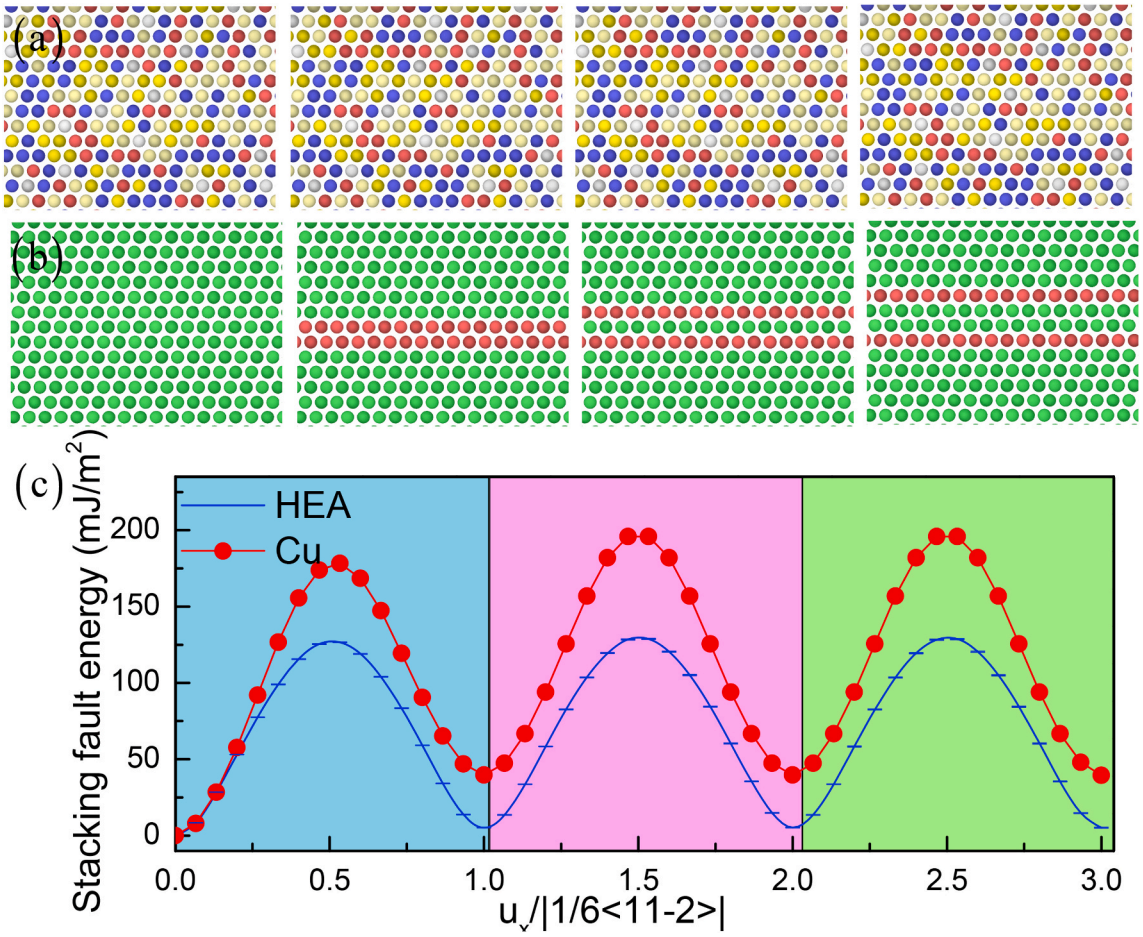

Fig. 3. Initial structure, intrinsic stacking fault, extrinsic stacking fault, and three-layer twin of the HEA (a, b). The atoms of the HEA are colored according to the atom type (a), and according to the CNA (b). SFE of the pure Cu, and average SFE of the HEA obtained from the 10 independent samples (c). The u_x stands for the moving distance. The initial structure corresponds to the moving distance of 0.0, the intrinsic stacking fault corresponds to the moving distance of 1.0, the extrinsic stacking fault corresponds to the moving distance of 2.0, and the three-layer twin corresponds to the moving distance of 3.0. Here, in the HEA, the energy of the intrinsic stacking fault is 5.10 mJ/m^2, the energy of the extrinsic stacking fault is 5.21 mJ/m^2, and the energy of the twin boundary is 5.11 mJ/m^2.

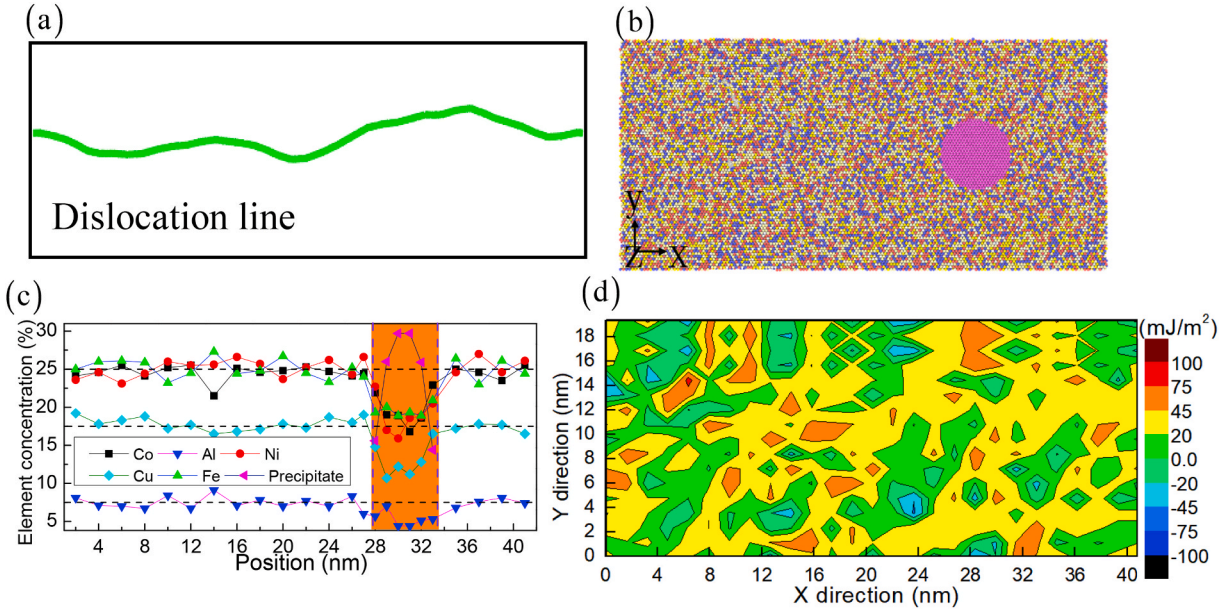

Fig. 4. (a) The schematic of a wiggled dislocation line in the distorted HEA lattice. (b) The distribution of various elements along the slip plane. The atoms are colored based on the atom type. (c) The concentration of the corresponding elements. The orange band represents the elemental concentration in the precipitate. (d) A random SFE landscape, and the corresponding average SFE of 5.10 mJ/m^2. (For interpretation of the references to color in this figure legend, the reader is referred to the Web version of this article.)

Table 1
The atomic radii of different type elements in the $Co_{25}Ni_{25}Fe_{25}Al_{7.5}Cu_{17.5}$ HEA.

Materials	Al	Co	Fe	Cu	Ni
Value (Å)	1.43	1.26	1.24	1.28	1.25

dislocation is 15 nm (Fig. 1a).

2.2. Shear deformation

To investigate the shear deformation, the *x* and *y* directions are set as the periodic-boundary conditions. The z direction is set to the free condition (Bacon et al., 2009; Rao et al., 2017b; Nöhring and Curtin, 2017), where the atoms within several layers at the top and bottom surfaces have the fixed z-coordinates. All MD simulations with the time step of 1 fs are performed with the open-source LAMMPS code (Plimpton, 1995). The sample system is created in the annealed state. For the annealed system, it is relaxed at 800 K for 100 ps followed by cooling to 300 K. This process could overcome barriers followed by gradual cooling (annealing) to reach the low energy regimes (Kirkpatrick et al., 1983), which is widely used for obtaining the optimal crystal structure. Here, such a computational annealing treatment reflects the experimental low-temperature annealing (typically around 0.2 ~ 0.3 Tm) or the recovery treatment (Wang et al., 2004). The local chemical short-range order is formed in the HEA matrix (see Fig. 3 and S1-S9), which agrees with the recent experiment (Zhang et al., 2020; Yin et al., 2020).

Then, the annealed sample is carried out in two stages, including the relaxation and deformation. The relaxation stage involves two different steps. Initially, the atom velocities of the HEA and precipitate are set randomly, based on the Maxwell-Boltzmann distribution. Secondly, MD simulations run for 100 ps using the isothermal–isochoric (NVT) ensemble at the target temperatures (10 K, 150 K, 300 K, 500 K, 800 K, and 1,200 K), followed by a relaxation for 100 ps using the isothermal-isobaric (NPT) ensemble at the target temperatures. Whereas in the second stage, the shear deformation is applied by displacing atoms with a speed of 0.15 m/s in the loading layer (Fig. 1a), imposing a shear strain rate of about 1×10^7 s^{-1} (Bacon et al., 2009). Meantime, this stage is simulated using a NVT ensemble. Although the hydrostatic stress occurs in the NVT ensembles at the finite temperatures due to the thermal expansion, its influence on the stress is negligible because the stress for the edge dislocation to overcome the precipitate is very high, relative to the stress induced by the thermal expansion (Singh et al., 2011a,b; Kuronen et al., 2015; Poschmann et al., 2018; Esteban-Manzanares et al., 2019a, b). Moreover, the strategies of the current simulation methods are widely used to investigate the dislocation-precipitate interactions in a wide temperature range (Singh et al., 2011a,b; Kuronen et al., 2015; Poschmann et al., 2018; Esteban-Manzanares et al., 2019a, b). Here, the software 'Ovito' is adopted to visualize the evolution of the atomic structure (Stukowski, 2009). The common neighbor analysis (CNA) is employed to analyze the local atomic structure, where the atoms "●" represent the FCC structure,

the atoms "○" are the unknown structure, the atoms "●" are the hexagonal-close-packed (HCP) structure, and the atoms "●" are the body-centered-cubic (BCC) structure. The dislocation extraction algorithm (DXA) is employed to represent the defects in the crystal in the form of a line-based dislocation network (Stukowski et al., 2012).

2.3. Distribution of element and stacking fault energy

Here, the different type atoms are randomly distributed, resulting in the HEA with a low SFE. The atomic model of the HEA is built, based on the low SFE principle in the following way. For each HEA model, we begin with the pure Co rectangular simulation cells and randomly replace Co atoms with Ni, Fe, Al, and Cu atoms up to a specified concentration, which agrees with the given elemental composition from the previous experiment (Fu et al., 2016). Simultaneously, the HEAs meet the low SFE principle. Here, the wiggled dislocation line occurs in the distorted HEA lattice due to the severe atomic-scale-lattice distortion (Fig. 4a), which is also observed by the previous experiment (Lei et al., 2018). The distributions of various elements along the slip plane are presented in Fig. 4b, and the fluctuation for the concentration of the corresponding elements is shown in Fig. 4c. The trends of the dislocation configuration and elemental distribution agree with the previous studies (Yeh et al., 2004; Diao et al., 2017; Zhang et al., 2014; Gao et al., 2016; Osetsky et al., 2019; Rao et al., 2017b). The y-axis projection views of different elemental distributions show some segregations in the HEA. The elemental disorder induces the non-uniform distribution of SFE (Fig. 4d). Here, the negative SFE stands for that the formation of HCP stacking in an FCC structure is energetically favorable and releases system energy in the metastable FCC HEAs. The distribution of SFE can be obtained by such a way, in which the HEA is divided into 220 (22×11) rectangular regions along the dislocation-slip plane, and the average SFE in each region is calculated. The non-uniform distribution of SFE results in varying stacking fault widths and curved partial dislocation line structures.

2.4. Cu-rich precipitate

In the present work, the Cu-precipitate strengthened $Co_{25}Ni_{25}Fe_{25}Al_{7.5}Cu_{17.5}$ HEA is studied (Fu et al., 2016). The pervious results reveal that the Cu-enriched precipitate nucleates easily owing to its low formation energy (Wang et al., 2009; Santodonato et al., 2015; Zhuang et al., 2013). Furthermore, the spherical Cu-rich precipitate is always observed in the Cu-containing HEAs (Singh et al., 2011a, b; Xu et al., 2015; Praveen et al., 2012). Considering the difference of the mixing enthalpy between Cu and other elements, Cu has the positive mixing enthalpy or the small negative mixing enthalpy, compared to the other elements (Co, Ni, Al, and Fe) (Praveen et al., 2012). Hence, the spherical Cu precipitate is chosen for this study in the $Co_{25}Ni_{25}Fe_{25}Al_{7.5}Cu_{17.5}$ HEA. In addition, the mismatch of the HEA and precipitate, which stands for the deformation of the invariant lattice, is given by $\varepsilon = 2(a_{Cu} - a_{HEA})/(a_{Cu} + a_{HEA})$, where the lattice parameters of the precipitate, a_{Cu}, and the HEA, a_{HEA}, are 3.615 Å and 3.603 Å (Fu et al., 2016), respectively. Here, the mismatch of the HEA-precipitate interface system is 0.33%. Hence, it is easier to form the coherent precipitate due to a very low lattice mismatch, compared to the lattice mismatch of 1.5% in the Ni-based alloys with the coherent precipitate.

2.5. Lattice constant at given temperatures

The lattice parameter of the $Co_{25}Ni_{25}Fe_{25}Al_{7.5}Cu_{17.5}$ HEA at a given temperature can be determined as follow: (a) The lattice parameter, a_0, obtained from the previous experiment (Fu et al., 2016) is chosen to build the initial MD model of the HEA. Here, the length dimension along the x-direction of the MD model is L_0; (b) The MD system keeps the target temperatures (10 K, 150 K, 300 K, 500 K, 800 K, and 1,200 K). Here, a new model size, L_1, is obtained along the x-direction; (c) The new lattice parameter, a_1, is $a_1 = a_0 L_1 / L_0$ at a given temperature.

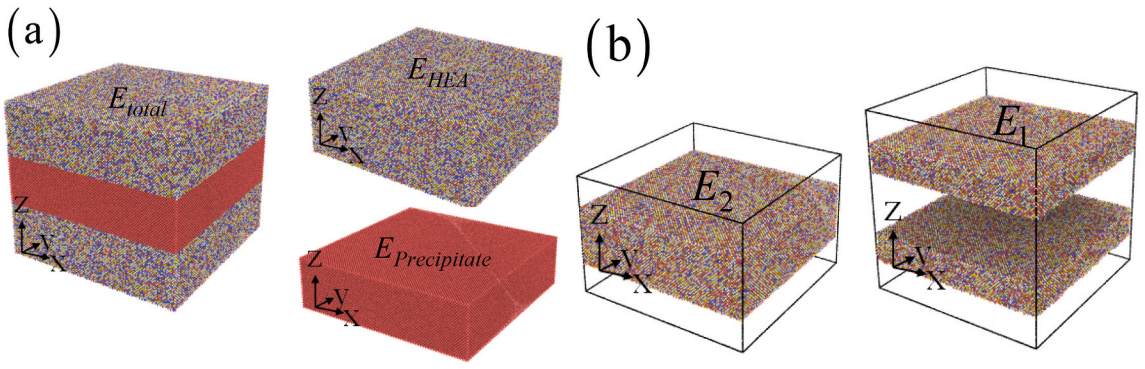

Fig. 5. (a) The model for calculating interface energy. (b) The model for calculating surface energy. Here, the atoms are colored, based on the atom type.

2.6. Interface and surface energies

To compute the interface energy between the HEA and Cu, the periodic-boundary conditions are employed in the x, y, and z directions at the temperature of 0 K (Fig. 5a). The size of the 'sandwich style' HEA-and-Cu model is 25.2 × 25.2 × 18 nm^3, the size of the HEA model is 25.2 × 25.2 × 11.5 nm^3, and the size of the Cu model is 25.2 × 25.2 × 6.5 nm^3. The three types of the crystallographic directions contain: (1) x - [1 0 0], y - [0 1 0], and z - [0 0 1], (2) x - [$\bar{1}$ 1 0], y - [0 0 1], and z - [0 1 1], and (3) x - [1$\bar{1}$0], y - [11$\bar{2}$], and z - [1 1 1], which correspond to the interfaces of (100), (110), and (111).

To compute the surface energy of the HEA, the periodic-boundary conditions are employed in the x and y directions, and the free-boundary condition is employed in the z direction at the temperature of 0 K (Fig. 5b). The size of the HEA model is 25.2 × 25.2 × 10.8 nm^3. The three types of the crystallographic directions contain: (1) x - [1 0 0], y - [0 1 0], and z - [0 0 1], (2) x - [$\bar{1}$ 1 0], y - [0 0 1], and z - [0 1 1], and (3) x - [1$\bar{1}$ 0], y - [11$\bar{2}$], and z - [1 1 1], which correspond to the surfaces of (100), (110), and (111).

3. Results

3.1. Effects of lattice distortion and precipitate

Introducing the precipitate is an effective strategy to provide the most significant contribution to the yielding strength, which has been demonstrated in the traditional alloys (Bacon et al., 2009; Jiang et al., 2017b). However, the synergistic effect of the severe lattice

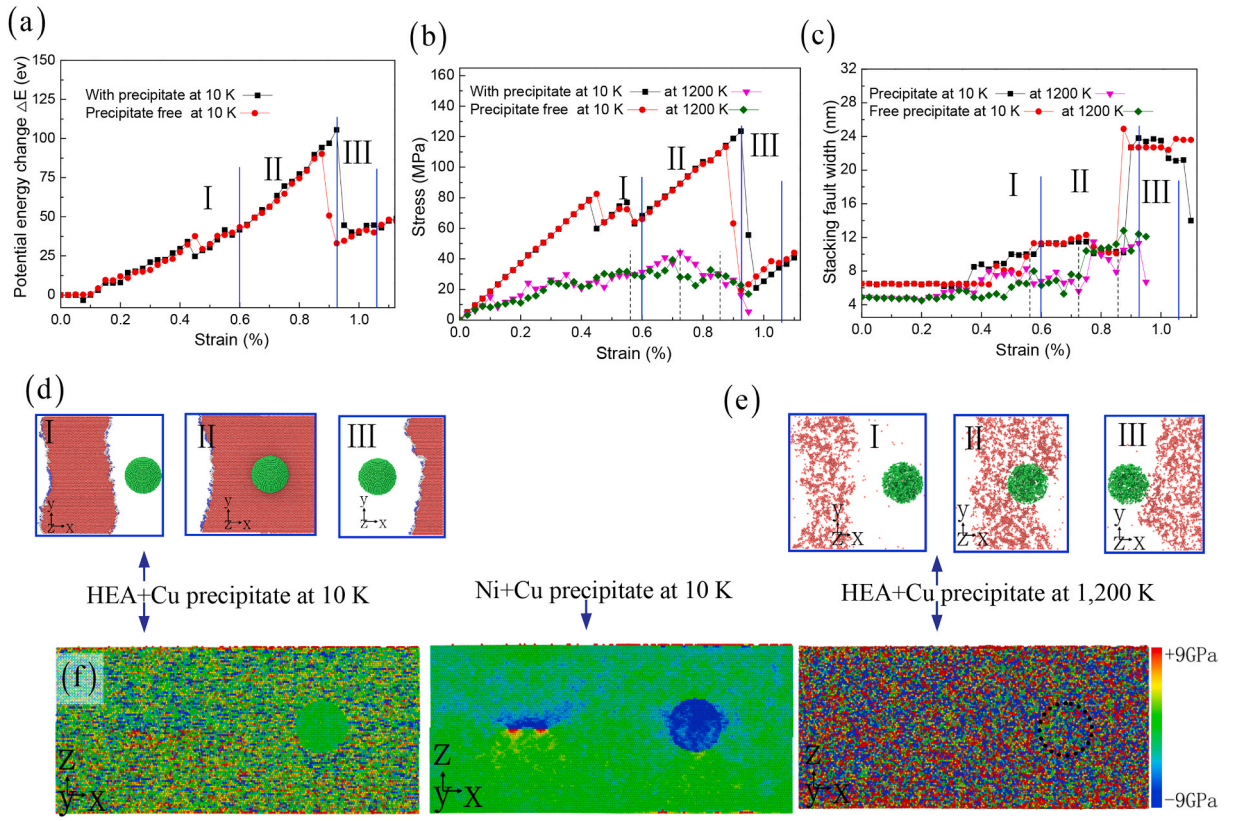

Fig. 6. (a) The potential energy change vs. the shear strain in the precipitate-strengthened HEA and the precipitate-free HEA at the temperatures of 10 K. (b) The shear stress versus the shear strain in the precipitate-strengthened HEA and the precipitate-free HEA at the temperatures of 10 K and 1,200 K, respectively. According to the relative position between the leading partial dislocation and precipitate at the temperature of 10 K, the regions are divided into 'I', 'II', and 'III' in the precipitate-strengthened HEA. (c) The stacking-fault width as a function of strain at the temperatures of 10 and 1,200 K, respectively. The regions are divided into 'I', 'II', and 'III' based on the relative position between the leading partial dislocation and precipitate at the temperature of 1,200 K in the precipitate-strengthened HEA. The dislocation interacting with a coherent precipitate at the temperatures of 10 K (d) and 1,200 K (e). This process includes the trapping of the leading partial dislocation, the stacking-fault-cutting precipitate, the trailing partial dislocation cutting precipitate, and the depinning of the trailing partial dislocation. "⚪" unknown structure, "🔴" HCP structure, and "🔵" BCC structure according to CNA (d, e). To highlight the precipitate, the corresponding atoms are colored by green ("🟢" precipitate atom). (f) The distribution of the shear stress τ_{xz} for the precipitate-strengthened HEA at the temperature of 10 K, for the precipitate-strengthened Ni at the temperature of 10 K, and for the precipitate-strengthened HEA at the temperature of 1,200 K. The atoms are colored based on the stress value. (For interpretation of the references to color in this figure legend, the reader is referred to the Web version of this article.)

distortion and precipitate strengthening on the HEAs has not been well understood (He et al., 2016; Yao et al., 2018; Gwalani et al., 2016; Xu et al., 2015; Wang et al., 2016; Ma et al., 2017). To verify the precipitate strengthening effect in the HEA, the relationships of the energy change or the stress with the shear strain are shown in Fig. 6a and b. Here, the potential energy change ΔE means the change of the system potential energy (See, Fig. 6a). It suggests that the dislocation-precipitate interaction is short-ranged due to the rapid decline of the potential energy change after the dislocation moving through precipitate. In addition, the dips in the potential energy curve stand for the local softening due to the chemical disorder. This fact has been proved by experiments, which show that elements have greater aggregation with the incipient concentration waves to cause the nanoscale alternating tensile and compressive strain fields (Ding et al., 2019). The atoms are deviating from the perfect lattice position owing to the atom radius difference, as presented in Fig. 1(c and d). The random distribution of atoms with various atomic radii (Table 1) induces the severe atomic-scale lattice distortion.

The atomic-size-difference parameter, δ_r, is calculated using the equation of $\delta_r = \sqrt{\sum c_i(1 - r_i/\bar{r})^2}$ (Zhang et al., 2008, 2014; Gao et al., 2016; Wu et al., 2019; Senkov et al., 2014), where c_i is the atomic fraction of the element of i in the alloys, $\bar{r}$ is the average atomic radius, and r_i is the atomic radius of the element of i. The atomic-size-difference parameter in the current $Co_{25}Ni_{25}Fe_{25}Al_{7.5}Cu_{17.5}$ HEA is 3.66%, which is larger than 2.07% in the CrMnFeCoNi HEA (Gludovatz et al., 2014), and smaller than 6.77% in the NiTiFeAlCu HEA (Jiang et al., 2017a).

In Fig. 6c, the local lattice distortion results in the fluctuation of the stacking fault width as the strain increases. The stacking fault strengthening is attributed to the chemical interaction between the stacking faults and solute atoms (Fig. 6c). The severe atomic-scale lattice distortion also leads to the interwoven region of the local tensile and compressive stresses (Fig. 6f), which cause the curved dislocation line (Fig. 1b) (Osetsky et al., 2019; Rao et al., 2017b; Nöhring and Curtin, 2017). Some kinks in the dislocation line form in the HEA (Figs. 1b, 6d, 6e), while the initially-straight dislocation line is observed in the pure Ni with a coherent Cu precipitate (Fig. 7). Especially, the interaction of the precipitate and dislocation in the pure Ni presents a strong-pair coupling case, which shows that there may be two paired dislocations entering inside the precipitate simultaneously (Fang et al., 2019). However, the interaction of the precipitate and dislocation in the HEA shows the weak-pair coupling case, which demonstrates that there are some faulted precipitates between two paired dislocations (Fang et al., 2019). Furthermore, the curved dislocation line with some kinks can interact with more solute atoms, to further increase the resistance of the dislocation motion. The curved dislocation changes from one to another states (Fig. 8), with the aid of the high applied stress required for overcoming the energy barriers (Diao et al., 2017; Zhang et al., 2014; Gao et al., 2016).

The precipitate-strengthening behavior is depicted in Fig. 6a and b, where the high critical stress at low or high temperatures occurs in the precipitate-strengthened HEA (Zhang et al., 2018b; Zhao et al., 2018; Yang et al., 2018b; Liang et al., 2018; Fu et al., 2018). Compared to the case of the precipitate-free HEA, the critical stress of the precipitate-strengthened HEA exceeds 9% and 12% at the low and high temperatures (Fig. 6b), respectively. When the dislocation is close to the precipitate, the stress changes significantly owing to the strong stress produced by the eigenstrain from the precipitate-matrix interaction (Fig. 6f). At the high temperature, the contribution of the total stress from the eigenstrain would reduce owing to the high lattice distortion and atomic diffusion to cause the large local stress (Fig. 6f). The severe atomic-scale lattice distortion produces a new phenomenon: (1) the high tensile and compressive stress fields are formed in the multiple-connected and single-connected regions; (2) the point-like low stress fields appear in the interior of the high stress region (Fig. 6f). Compared to the conventional precipitate-strengthened alloys (Yang et al., 2018a), the low/free stresses occur in the precipitate, to reduce the energy of the dislocation core when the dislocation-bypassing precipitate (Fig. 1e). At

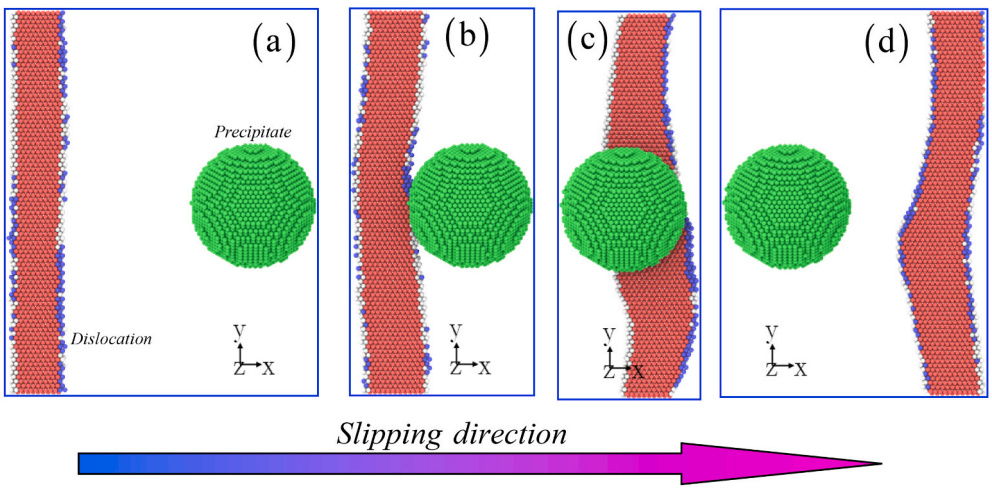

Fig. 7. The dislocation interacting with a coherent Cu precipitate in the pure Ni at different strains: 0% (a), 4% (b), 4.5% (c), and 5% (d). The full dislocation broken down into the partial dislocations (a), the trapping of the leading partial dislocation (b), just before the depinning of the leading partial dislocation (c), and the depinning of the trailing partial dislocation (d). "⚪" unknown structure, "🔴" HCP structure, and "🔵" BCC structure according to CNA. To highlight the precipitate, the corresponding atoms are colored by green ("🟢" precipitate atom). (For interpretation of the references to color in this figure legend, the reader is referred to the Web version of this article.)

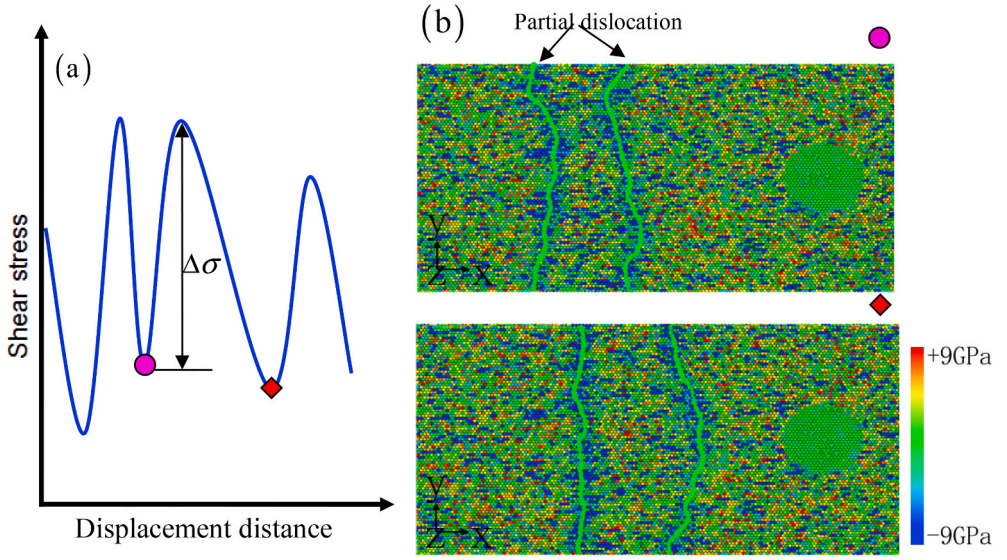

Fig. 8. (a) The schematic diagram of the resistance to overcome from one to another state of the dislocation (●→◆). (b) The bow of the partial dislocation occurs due to the complex stress τ_{xz}. The symbols of ● and ◆ indicate two states of the curved dislocation motion. The green line stands for the partial dislocation line. $\Delta\sigma$ represents the overcome resistance from the state of '●' to the state of '◆'.

low and high temperatures, the severe atomic-scale lattice distortion increases the shear stress during the initial stage of the dislocation movement, and the precipitate-dislocation interaction governs the shear stress during the dislocation-cutting-precipitate stage (Yang et al., 2018b; Liang et al., 2018; Fu et al., 2018).

The width of stacking fault in the HEA is measured in Fig. 6c. As a result, the change of the shear stress strongly affects the stacking fault width, especially when the dislocation is close to the precipitate. The stacking fault would contribute to strengthening due to the obvious difference of SFE between the HEA and precipitate (within the inner of the HEA matrix) (Fig. 3), which causes the stacking fault bending at the precipitate-HEA interface. Moreover, the stacking fault width not only relies on the local SFE (Fig. 4d), but also depends on the increase strain. Fig. 7c and d reveal that the fluctuation of the stacking fault width affects the energy barrier for the partial dislocation motion.

3.2. *Effect of chemical disorder*

The chemical disorder with an increase number of the principal elements, and/or the altered concentrations of the specific

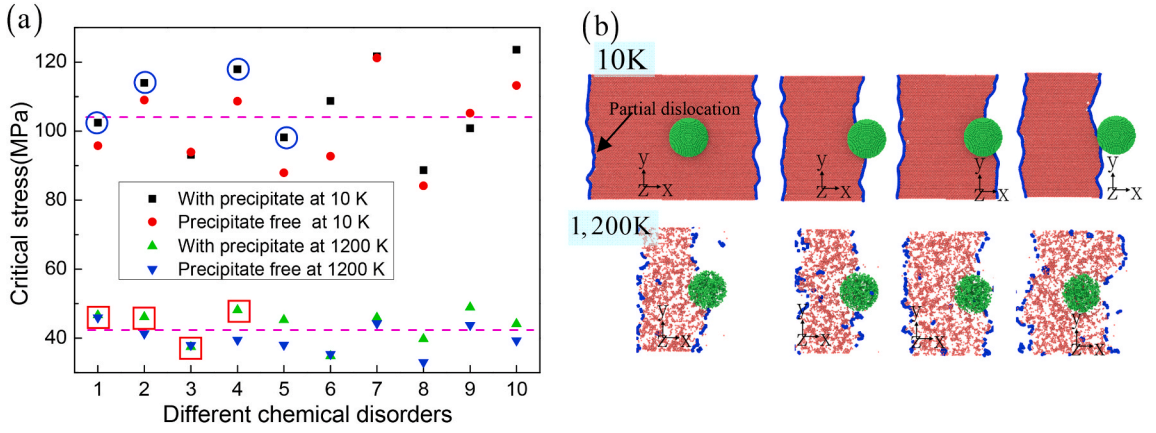

Fig. 9. (a) The critical stress vs. chemical disorder, where the precipitate size is 3 nm. (b) The dislocation interacting with the coherent precipitate for different chemical disorders at the temperatures of 10 and 1,200 K. The microstructures in the symbols of and are analyzed in (b). "○ and □" HCP structure according to CNA. To highlight the precipitate, the corresponding atoms are colored by green ("○ and □" precipitate atom). The blue line represents the partial dislocation line. (For interpretation of the references to color in this figure legend, the reader is referred to the Web version of this article.)

elements, and/or the changed distribution of elements in the single-phase concentrated solid-solution alloys can lead to the substantial fluctuation of SFE (Zhao et al., 2019; Zhang et al., 2015; Ding et al., 2018a; Ikeda et al., 2018; Suzuki, 1952). Furthermore, the low SFE of the HEA depends upon the chemical composition, and has a major influence on its plasticity by the following mechanisms: (i) partial and perfect dislocation gliding, (ii) mechanical twinning, and (iii) phase transformation. Here, 10 independent samples with a random occupation of the five chemical elements over the sites of an FCC structure have been used as initial conditions for the MD simulations (Zhao et al., 2019; Ding et al., 2018a). The corresponding average SFEs are 6.37, 5.61, 5.39, 5.62, 4.95, 5.26, 5.75, 5.41, 5.38, and 5.10 mJ/m^2, respectively (Figs. S1–S9).

Fig. 9a shows the fluctuation of the critical stress in the samples with different element distributions, which is irrelevant to the average SFE. Here, the critical stress of the precipitate-strengthened HEA is generally 1.08 and 1.12 times larger than that in the precipitate-free HEA at low and high temperatures in addition to the precipitate softening effect, respectively. Here, the weak-pair coupling case for the interaction of the precipitate and dislocation takes place in the HEA, which provides a small contribution to the critical stress compared to the solid-solution strengthening (Fang et al., 2019). Thus, the chemical disorder can contribute significantly to the critical stress, which can dominate the strengthening behaviour in the precipitate-strengthened HEA. The microstructure at the critical stress is presented in Fig. 9b. Based on the thermodynamics of stacking faults, the decrease of SFE results in the extension of the dissociation width when the solute segregates into the stacking fault (Suzuki, 1952). The present study reveals the occurrence of the stacking fault fluctuation in the independent samples, which depends on the local SFE. Interestingly, in some cases, the "softening" effect can be observed in the precipitate-strengthened HEAs at low temperatures. As the temperature increases to 1200 K, the extent of interactions between the dissociated dislocations and precipitates becomes more pronounced, due to the fact that the narrower dissociation of the dislocations occurs at elevated temperatures. After a dislocation cuts into a coherent precipitate, it leaves an APB on the slip plane in the HEAs. Considering a straight dislocation segment of a length L traveling normal to the segment n at a distance, the APB energy of the swept area is expressed as $E_{\mathrm{APB}} = \chi_{\mathrm{APB}} Ln$, where χ_{APB} is the APB energy per unit area. Moreover, the resistance of the dislocation movement is reduced due to the low lattice distortion and low dislocation-slip resistance in the interior of the precipitate, and the corresponding reduced energy is $E_{\mathrm{precipitate}}$. Thus, the resistance work from the precipitate is the difference value of $\Delta = E_{\mathrm{APB}} - E_{\mathrm{precipitate}}$, compared with the precipitate-free HEA. Hence, the nanoscale chemical disorder seems to be responsible for controlling the strengthening and softening mechanisms in the precipitate-strengthened HEAs.

3.3. *Effects of precipitate spacing and size*

In the classical precipitate strengthening theory, the critical stress depends on the spacing and size of the precipitate (Bacon et al., 2009). It is noted that the simulated box size increases and the precipitate size with a radius of 3 nm keeps constant in Fig. 10a (Zhou et al., 2011), where the precipitate spacing is 2.5, 6.5, 10, 13.5, 17, 20.5, 24 nm; and the precipitate size increases and the simulated box size keeps constant in Fig. 10b (Zhou et al., 2011), where the precipitate sizes are 1, 2, 3, 4, 5, 6, 7, and 8 nm. As the precipitate spacing increases, the critical stress firstly increases, and then decreases at the low temperature of 10 K. Especially, at the precipitate spacing larger than 5 nm, the precipitate strengthening effect becomes very weak, agreeing with the previous work (Bacon et al., 2009). However, the critical stress firstly decreases, and then keeps stable at the high temperature of 1,200 K. It can be found that the precipitate can always enhance the strength of HEA at the temperature of 10 K with the increase distance between precipitates (Fig. 10a). Here, at the temperatures of 10 K and 1,200 K, the critical stress exceeds 7.5% and 7.7% than that in the precipitate-free HEA, regardless of the precipitate softening.

To further investigate effect of the precipitate spacing on the critical stress, we also compare the other two models with MD simulations. For the coherent Cu precipitate, dislocation pairs cutting through precipitates are usually weakly coupled, and the critical

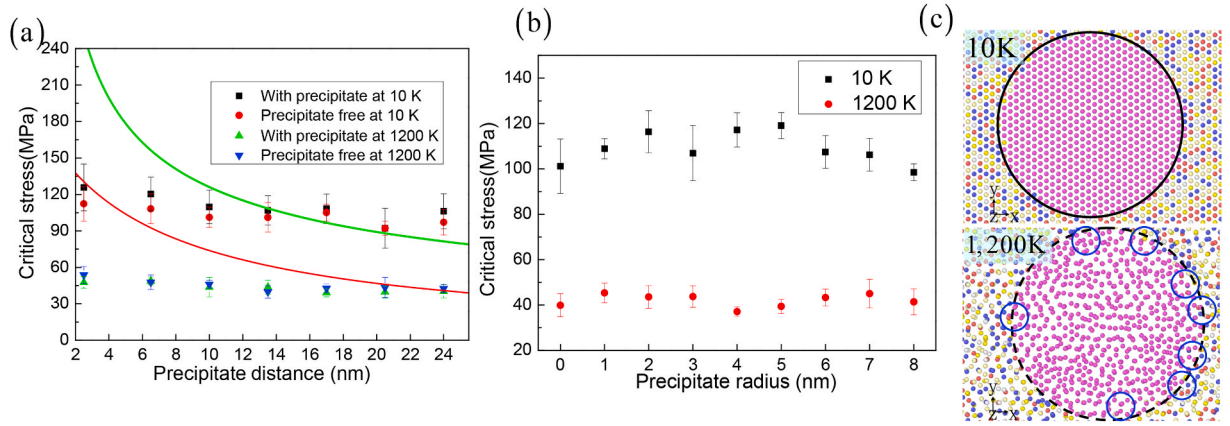

Fig. 10. (a) The critical stress vs. distance between precipitates. (b) The critical stress vs. precipitate size. (c) Atomic diffusion at the HEA-precipitate interface at the high temperature of 1,200 K and precipitate radius of 3 nm. The black solid and dotted circles represent the interface between HEA matrix and precipitate at the temperature of 10 K and 1,200 K.

stress required for dislocation movement can be estimated by (Brown and Ham, 1971) $\tau_{cutting} = \frac{\gamma_{APB}}{2b}\left[\left(\frac{2\gamma_{APB}df}{\pi T}\right)^{1/2} - f\right]$, where $\gamma_{APB} = 0.32$ J/m^2 is the average value of the APB energy, b = 0.249 nm is the Burgers vector of the dislocation, $d = 2r$ is the average diameter of the sheared precipitates in the gliding plane, r is the radius of the precipitate, f is the volume fraction of the precipitates, and T is the dislocation line tension, which can be approximated as Gb^2/2. G = 74 GPa is the shear modulus of the HEA matrix. On the basis of work from Bacon, Kocks and Scattergood (BKS), the critical stress required for an edge dislocation to bypass a regular array of inclusions can be written as (Bacon et al., 1973) $\tau_{BKS} = \frac{Gb}{2\pi L}\left[\ln\left(\frac{2rL}{2r+L}\right) + B\right]$, where G is the shear modulus of the HEA matrix, b is the Burgers vector of the dislocation, r is the radius of the precipitates, L is the distance that separates the centers of precipitates, and B is an adjustable parameter. For this two models, the critical stress predicted by the dislocation-cutting-precipitate model is closer to the MD simulation result, compared with the BKS model for the dislocation-looping-precipitate. However, the obvious difference in the critical stress obtained from the atomic simulation and theoretical model is observed due to the severe lattice distortion effect. Here, the Cu precipitate as a soft metal phase is essentially transparent to dislocations, and thus its strengthening is particularly limited. This trend can explain why Brown and BKS model are completely off when predicting an effect of the distance between precipitates on the critical stress. Therefore, this result is different from the classical hard phase strengthening, such as multicomponent intermetallic nanoparticles (Yang et al., 2018b).

Fig. 10b shows that the critical stress firstly increases, and then decreases with the increase precipitate size at the low temperature. The large precipitate with less lattice distortions reduces the solid solution strengthening. However, at high temperatures, the solute atoms diffuse into the precipitate (Fig. 10c), which enhances the lattice distortion to impede the dislocation motion. Hence, compared to the precipitate-free HEA, the critical stress fluctuates with the increase precipitate size at high temperatures, due to the strong barrier for the dislocation slip in the precipitate embedded by the solute atom. Compared to the traditional alloys, the stacking fault width is large due to the low SFE of the HEA (Fig. 11), and the short-range effect of the stress field between the dislocation and solutes is strong due to the severe atomic-scale lattice distortion (Gao et al., 2016). When a diameter of the precipitate is smaller than the stacking fault width in the HEA, the leading dislocation always bypasses the precipitate by the cutting process (Fig. 11). This reason could lead to reducing the precipitate strengthening effect for different precipitate spacings and sizes.

3.4. Effect of temperature

The critical stress during the dislocation-precipitate interaction at different temperatures is presented in Fig. 12a. As compared with the traditional metals and alloys (Kotrechko et al., 2015; Iskandarov et al., 2011), the HEAs exhibit a temperature dependence of the critical stress, which has a relatively small downward trend with the increase temperature. Fig. 12a shows that the higher critical stress occurs at cryogenic temperatures. This result is consistent with the experimental data, where the CrMnFeCoNi HEA exhibits a high yield strength at a low temperature of 77 K (Gludovatz et al., 2014).

For a high-temperature environment, the HEA presents the relatively-high strength and has no obvious weakening behavior

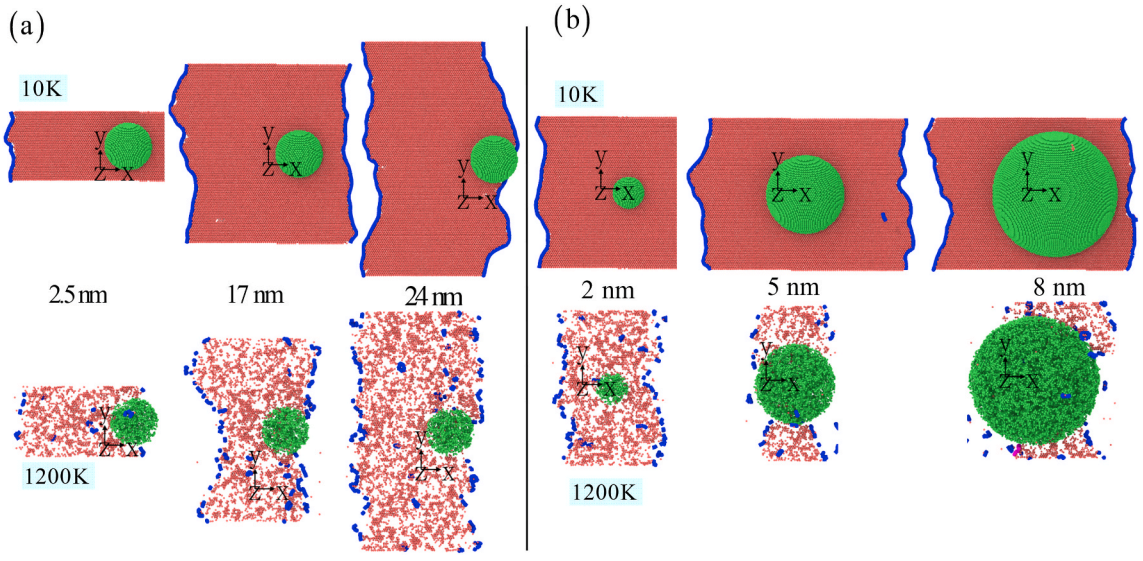

Fig. 11. (a) The dislocation interacting with the precipitate at the precipitate spacings: 2.5, 17, and 24 nm. (b) The dislocation interacting with the precipitate at the precipitate sizes: 2, 5, and 8 nm "🔴" HCP structure according to CNA. To highlight the precipitate, the corresponding atoms are colored by green ("🟢" precipitate atom). The blue line represents the partial dislocation line. (For interpretation of the references to color in this figure legend, the reader is referred to the Web version of this article.)

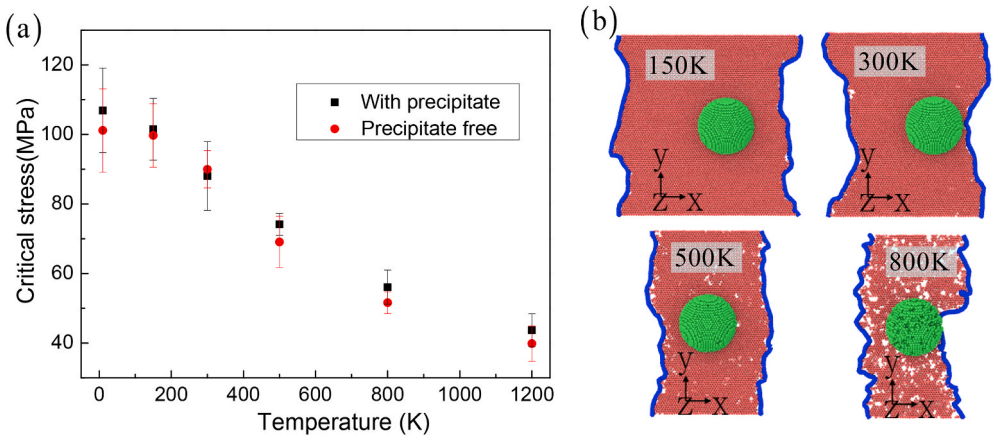

Fig. 12. (a) The temperature dependence of the critical stress at the temperatures of 10, 150, 300, 500, 800, and 1,200 K in the precipitate-strengthened and precipitate-free HEA. The precipitate size is 3 nm, and precipitate spacing is 13.4 nm. (b) The dislocation interacting with a coherent precipitate at the temperatures of 150, 300, 500, and 800 K "🔴" HCP structure according to CNA. To highlight the precipitate, the corresponding atoms are colored by green ("🟢" precipitate atom). The blue line represents the partial dislocation line. (For interpretation of the references to color in this figure legend, the reader is referred to the Web version of this article.)

(Fig. 12a). This trend is consistent with the observation of the previous experiments Zou et al. (2015); Huang et al. (2017); Jiang et al. (2017a); Yang et al. (2018b). However, for the pure metal at elevated temperatures, the atomic bonds are obviously weakened regardless of whether the atom spacings increase or decrease, which lead to a sharp decline in the strength (Iskandarov et al., 2011). When the dislocation passes through the coherent precipitate, APB still generates at high temperatures and causes the strong barrier to the dislocation glide. The stacking fault width relies on the increase temperature (Huang et al., 2015), and the enhanced lattice distortion hinders the stacking fault to widen (Fig. 12b). The higher temperature produces the lattice distortion in the stacking fault, to increase the dislocation-sliding resistance. The structural integrity and shape of the precipitate depend upon the temperature (Fig. 12b). Compared to the FCC FeCrNi alloys and metals at the equal homologous temperatures, the slow diffusion takes place in the HEAs, due to the lattice-distortion-generated deep stress trap along the diffusion path for an atom in the lattice (Diao et al., 2017; Zhang et al., 2014; Gao et al., 2016; Miracle and Senkov, 2017). This trend results in the relatively stable structure of the precipitate at high temperatures (Zou et al., 2015; Huang et al., 2017; Jiang et al., 2017a) to improve the strength of the HEAs. On the other hand, the non-connected local high stress field (Fig. 6e) would limit the free diffusion, and even lock some atoms in the high stress area to hinder the dislocation motion.

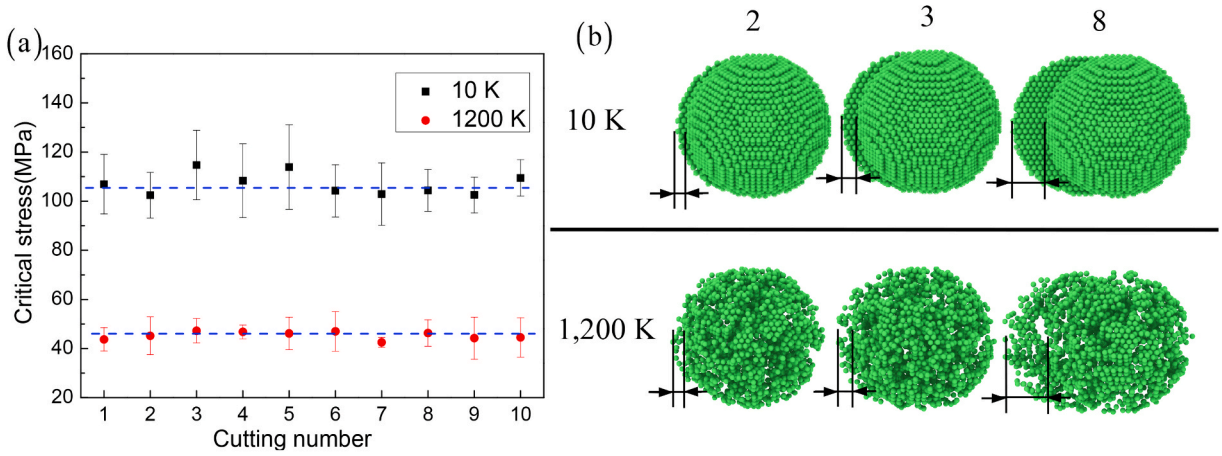

Fig. 13. (a) The dislocation-cutting-number dependence of the critical stress at the temperatures of 10 and 1,200 K in the precipitate-strengthened HEA, where the precipitate size is 3 nm. (b) The precipitate shape after the dislocation bypassing the precipitate at dislocation-cutting numbers of 2, 3, and 8, and at the temperatures of 10 K and 1,200 K "🟢" represents the atom of the precipitate. With the increase of dislocation-cutting numbers, the width of APB increases. If a domain adjoins another domain of different types, APB is formed between them. The APB is formed perpendicular to a crystal-plane orientation of {111} in the precipitate-strengthened HEA. The distance between the black lines with the arrow presents the width of APB. At the temperature of 1,200 K, the multiple dislocation-cutting process reduces the structural integrity of the precipitate.

3.5. Effect of dislocation-cutting number

At low temperatures, the increase dislocation-cutting number results in a slight fluctuation of the stress (Singh and Warner, 2010), due to the decrease of the dislocation-cutting-precipitate region (Fig. 13). Here, the dislocation-cutting number is defined as the number of dislocations that have sheared the precipitate. The width of APB increases with the increase of the dislocation-cutting number, which leads to a higher shear stress. The recent experiments (Zhang et al., 2018b; Zhao et al., 2018; Yang et al., 2018b; Liang et al., 2018; Fu et al., 2018) also show that the strengthening of dislocation-cutting-precipitate plays an important role in the strength of the HEAs. The stress relies on the competition relationship between the decrease cutting radius and the increase APB width (Fig. 13b). However, at high temperatures, the stress keeps stable with the increasing dislocation-cutting number (Fig. 13a), owing to the weakening effect of APB. Once the dislocation cuts into the precipitate, the slip resistance of the partial dislocation decreases. This trend is due to that the absence of the lattice distortion in the coherent precipitate generates a low stress region (Fig. 1e). Hence, the critical stress depends upon the competition between the strengthening by APB and the softening by the annihilation of the lattice distortion.

3.6. Elemental segregation around the interface

Some reports show that elemental segregation occurs around the interface between the precipitate and matrix, and would affect the dislocation-precipitate interaction (Middleburgh et al., 2014; Lin and Tsai, 2011; Singh et al., 2011a,b; Shin et al., 2017). Importantly, in-depth understanding segregation behaviour around the interface is conducive to the successful alloy design and the optimum thermomechanical treatments, for achieving the desired mechanical properties of the HEAs. Here, the Co (Fe, Ni, Al) elemental segregation around the interface is investigated, to reveal the segregation effect on the precipitate strengthening. The corresponding element concentration around the interface is increased by 15%, as shown in Fig. 14a. Considering the elemental segregation, the features of the long-range effect in the stress-strain curves can be ignored in Fig. 14b and c. The obvious stress change takes place at the highest stress peak points around the interface. The critical stresses for the dislocation-precipitate interaction are in the following order: no segregation > Ni segregation > Al segregation > Fe segregation > Co segregation at the temperature of 10 K. This trend is due to that the elemental segregation reduces the degree of the local lattice distortion. The critical stresses at the temperature of 1200 K are in the following order: Fe segregation > Co segregation > no segregation > Ni segregation > Al segregation. As shown in Fig. 14d, the elemental segregation would improve the high temperature stability of a precipitate (Shin et al., 2017), resulting in the increase of the critical stress.

4. Discussion

To reveal the difference of the severe atomic-scale lattice distortion at different temperatures (Fig. 1d), we calculate the parameter of the lattice distortion for the HEAs (Zhang et al., 2014; Gao et al., 2016; Wu et al., 2019) in the schematic diagram of Fig. 15a, which could be directly calculated from the local lattice parameter δ

$$\delta = \frac{1}{N}\sum_{i=1}^{N}\left[\frac{\mathrm{mod}(|x_i|, k_x a_i(T))}{k_x a_i(T)} + \frac{\mathrm{mod}(|y_i|, k_y a_i(T))}{k_y a_i(T)} + \frac{\mathrm{mod}(|z_i|, k_z a_i(T))}{k_z a_i(T)}\right] \quad (1)$$

where N is the atomic number of the HEA, $a_i(T)$ is the lattice constant at the temperature of T, and x_i, y_i, and z_i are the offset distances of i atom in the unit cell along the x, y, and z directions, respectively. k_x, k_y, and k_z are the numbers of the unit cell along the x, y, and z directions, respectively. Moreover, all the atoms are unable to move from one to another unit cell. Namely, the atom moves only in the initial unit cell (Fig. 15a).

Fig. 15b shows that the lattice distortion decreases quickly with the increase temperature in the HEA. At low temperatures, the atoms frozen in the initial position are difficult to release the lattice-distortion energy by diffusion. Thus, all atoms are extremely hard to return to their ideal positions. At high temperatures, the atoms rearrange the ideal equilibrium positions during the diffusion process. Hence, the stored strain energy and severe atomic-scale lattice distortion decrease. This trend reduces the degree of the lattice distortion at elevated temperatures, which is the fundamental cause of the high strength at cryogenic temperatures compared with the conditions of room and high temperatures (Gao et al., 2016; Zou et al., 2015; Jiang et al., 2017a). Moreover, the lattice constant expands obviously at high temperatures in Fig. 15c. This trend reduces the resistance of the dislocation glide, due to the cooperation of the thermal activation. Furthermore, the stacking fault width decreases at high temperatures (Huang et al., 2015), to weaken the stacking fault strengthening. The precipitate can easily diffuse into the HEA matrix at high temperatures, due to the decrease of the diffusion-energy barrier. The dissolving and weakening of the precipitate occur at high temperatures. As a result, the complete crystal structure of the precipitate is spontaneously broken, attributed to that the atoms in the HEAs move into the interior of the precipitate at high temperatures (Fig. 13b). Therefore, it could lead to a decrease of the strength in the HEAs at high temperatures. In other words, the original cause of the high strengths at cryogenic temperatures is attributed to the large atomic-scale lattice distortion frozen in the HEA matrix, to difficultly release the lattice-distortion energy by the diffusion. The origin of the high strengths at elevated temperatures is due to that the slow diffusion induced by the lattice-distortion-generated deep stress trap along the diffusion path results in the relatively-stable structure of the precipitate.

According to the results from the MD simulations, we consider different conditions for the dislocation-bypassing precipitate process based on the dynamical dislocation theory (Hirth and Lothe, 1982): (1) the leading dislocation-cutting precipitate should meet the

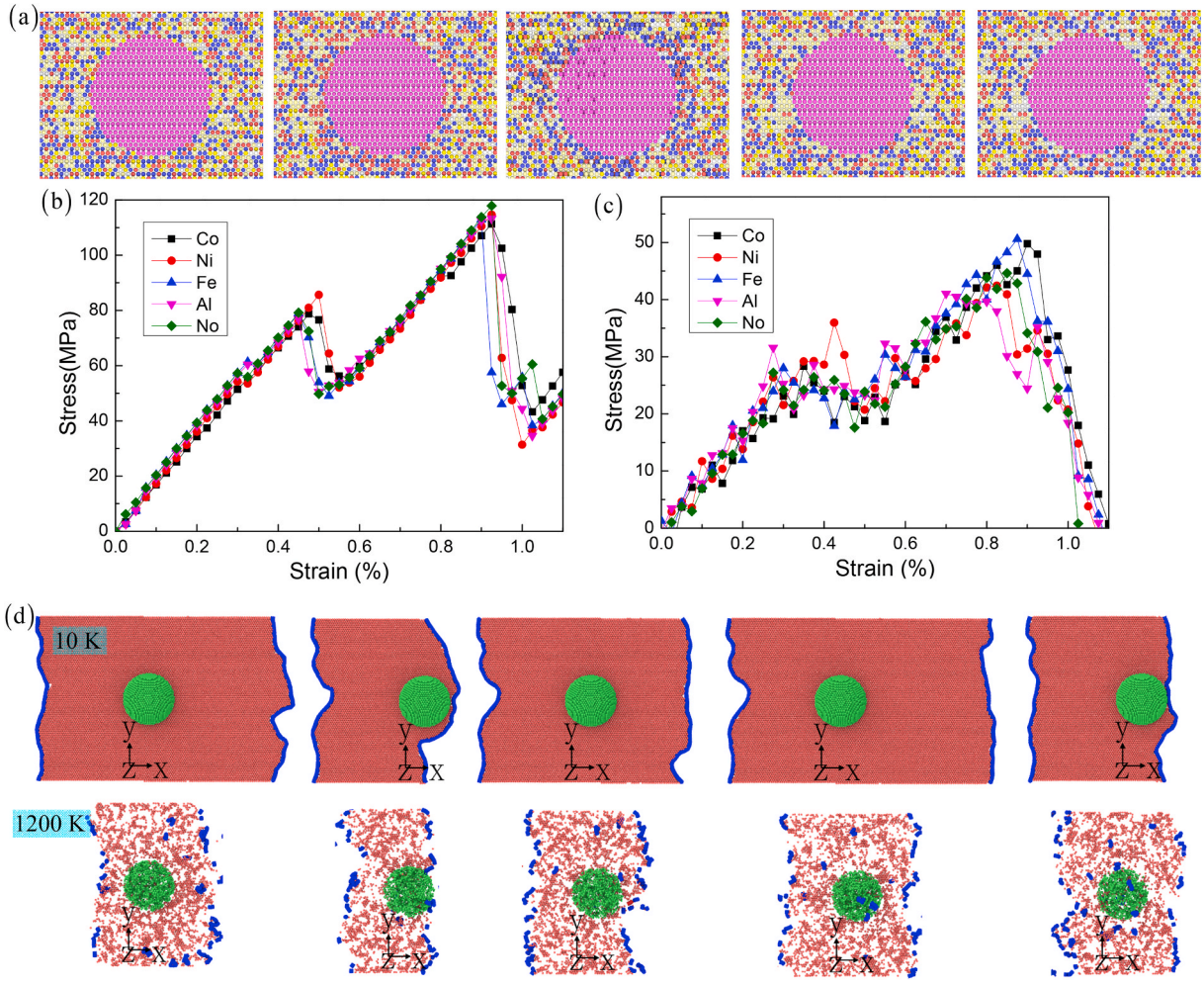

Fig. 14. Element distribution around the interface: no segregation, Co segregation, Ni segregation, Fe segregation, and Al segregation (a), where the precipitate size is 3 nm. The stress vs. strain in HEA with different elemental segregations at the temperature of 10 K (b), and 1200 K (c). The dislocation interacting with a coherent precipitate at the temperatures of 10 K and 1200 K (d). "" HCP structure according to CNA. To highlight the precipitate, the corresponding atoms are colored by green ("" precipitate atom). The blue line represents the partial dislocation line. (For interpretation of the references to color in this figure legend, the reader is referred to the Web version of this article.)

condition of the formula, $\sigma b = \gamma_2 - \gamma_1$, where b is the Burgers vector of the partial dislocation, σ is the external force, γ_2 is SFE with the atomic segregation, and γ_1 is SFE without the atomic segregation; (2) the trailing-dislocation-cutting precipitate should meet the condition of the formula, $\sigma b = \gamma_{ch} - \gamma_1$, where γ_{ch} is the surface energy; (3) the full-dislocation-cutting precipitate should meet the condition of the formula, $\sigma b = \gamma_2 - \gamma_1 + \gamma_{ch}$. Hence, SFE always plays a key role in the precipitate-strengthening mechanism by the process of the dislocation-cutting precipitate. Meanwhile, the critical stress required for the dislocation nucleation and emission depends on SFE of the metals and alloys (Gao et al., 2016; Kotrechko et al., 2015; Hirth and Lothe, 1982). On one hand, the severe atomic-scale lattice distortion of the HEA reduces SFE (Gao et al., 2016), to increase the probability of the partial dislocation nucleation. On the other hand, the alternating compressive-and-tensile stress fields along the dislocation line and the dislocation-motion path are produced by the severe atomic-scale lattice distortion (Figs. 4a and 8), to improve the resistance of the dislocation motion.

To study the stability of the precipitate-HEA interface, the interface energy is calculated in Fig. 5a, according to the equation of $E_{interface} = [E_{total} - (E_{Precipitate} + E_{HEA})]/(2S)$, where E_{total}, $E_{Precipitate}$, and E_{HEA} represent the energies of the precipitate-HEA system, the perfect precipitate, and the perfect HEA matrix, respectively. S is the surface area of the interface. The interface energies of (100), (110), and (111) calculated by MD simulations are 793 ± 31, 379 ± 34, and 320 ± 33 mJ/m^2, respectively. In the precipitate-strengthened Ni-based superalloy, the interface energies of (100), (110), and (111) are 46, 28, and 12 mJ/m^2, respectively. Hence, the interface energy in the precipitate-strengthened HEA is higher than that in the precipitate-strengthened Ni-based superalloy, due to the severe atomic-scale lattice distortion of the HEA (Mishin, 2004). The high interface energy increases the energy of APB, and then improves the strength of HEA. The precipitate-HEA interface energy with the orientation of {111} is low, meaning that the precipitate

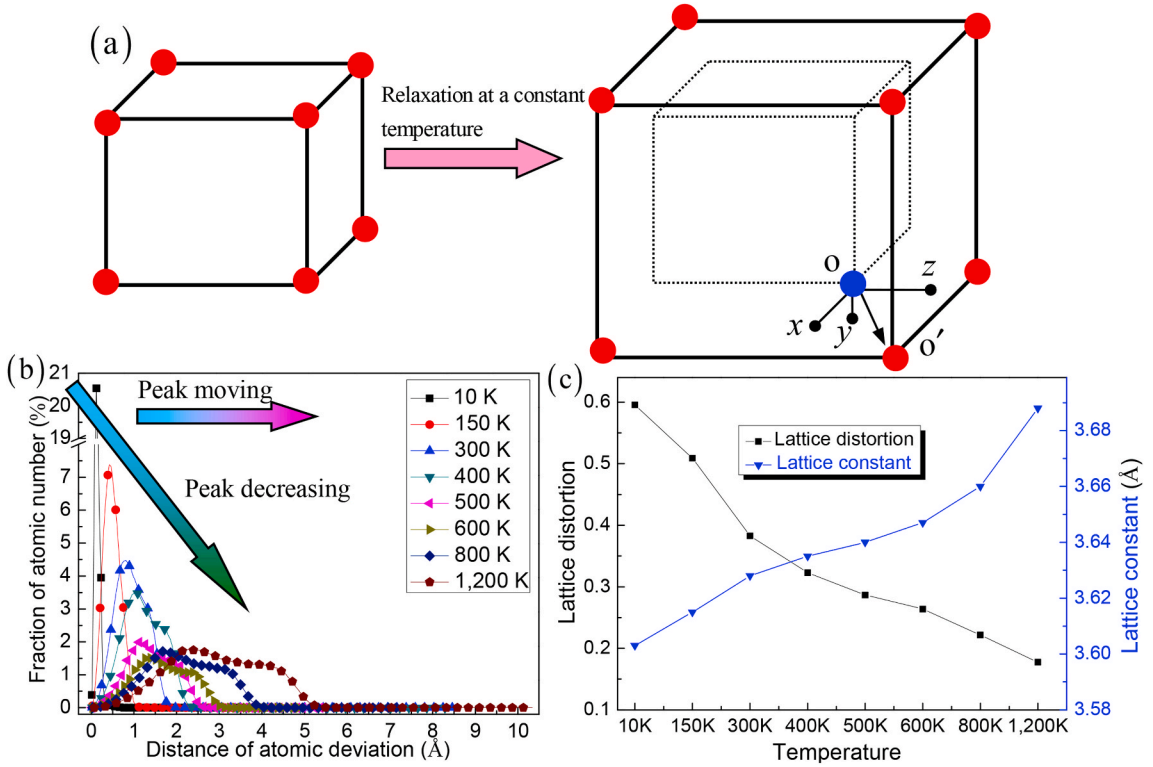

Fig. 15. (a) Schematic diagram of the distance of the atom deviation in a unit cell along the x, y, and z directions at various temperatures. (b) The fraction of the atom number vs. the distance of the atomic deviation. (c) The lattice constant vs. the temperature. The fraction of atom number means the ratio between the total atom number and the atom number at different deviation distances.

phase grows along the most favorable direction of <111>. Furthermore, the surface energy of the HEA also presents the interface stability in the precipitation process. The surface energy is calculated by the expression of $E_{surface} = (E_1 - E_2)/(2S)$ in Fig. 5b, where E_2 is the total energy of a perfect lattice with two surfaces, E_1 is the total energy of a perfect lattice with four surfaces, and S is the surface area. The surface energies of (100), (110), and (111) calculated by MD simulations are 1,714 ± 19, 1,871 ± 18, and 1,597 ± 17 mJ/m^2, respectively. The surface energy of the HEA with (111) is lower than the surface energies of other crystal surfaces of (100) and (110), which is in good agreement with the experiments and simulations in the FCC metals and alloys (Mishin, 2004; Foiles et al., 1986). The results of the above MD simulations reveal that the lattice distortion of the HEA can change SFE, interface energy, and surface energy, which sensitively affect the dislocation-precipitate interaction and determine the mechanical properties of the HEA.

5. Conclusion

In summary, the microstructural evolution of the complex interaction between the dislocation and coherent precipitate in the HEA has been examined, using MD simulations during the shear deformation. The effects of the temperature, chemical disorder, precipitate spacing and size, elemental segregation, and dislocation-cutting-precipitate number on the precipitate-strengthened behaviour are studied. As compared to the pure metals and alloys, the synergistic strengthening of the coherent precipitate and severe atomic-scale lattice distortion is revealed. The local lattice parameter predicted by our theoretical model is useful to understand the root cause of the low-temperature strengthening.

The effect of the change stacking fault width due to the obvious SFE difference between the HEA and precipitate (within the inner of the HEA matrix) contributes to the strength of the HEA. The low structural integrity and the precipitate embedded by the solute increase the dislocation slip resistance, to improve the strength at elevated temperatures. The critical stress depends upon the competition between the APB strengthening and the lattice-distortion-free softening. Moreover, the chemical disorder, precipitate spacing and size, elemental segregation and dislocation-cutting number play an important role in the critical stress and the dissociation and shape of the dislocation. Therefore, by adjusting the precipitate characteristics and the elemental ratio and distribution to control the local lattice distortion, the strong and tough advanced HEAs can be developed and desired for the extreme-environment applications.

CRediT authorship contribution statement

Jia Li: Investigation, Methodology, Validation, Visualization, Software, Writing - original draft, Writing - review & editing.

Haotian Chen: Investigation, Methodology, Validation, Writing - original draft, Writing - review & editing. **Qihong Fang:** Conceptualization, Investigation, Methodology, Validation, Visualization, Writing - original draft, Writing - review & editing, Project administration, Resources, Supervision. **Chao Jiang:** Conceptualization, Investigation, Methodology, Validation, Visualization, Writing - original draft, Writing - review & editing, Project administration, Resources, Supervision. **Yong Liu:** Conceptualization, Investigation, Methodology, Validation, Visualization, Writing - original draft, Writing - review & editing, Project administration, Resources, Supervision. **Peter K. Liaw:** Investigation, Methodology, Funding acquisition, Writing - review & editing, Project administration, Resources, Supervision.

Declaration of competing interest

The authors declare that they have no known competing financial interests or personal relationships that could have appeared to influence the work reported in this paper.

Acknowledgements

The authors would like to deeply appreciate the support from the Foundation for Innovative Research Groups of the National Natural Science Foundation of China (Grant No. 51621004), the NNSFC (11772122, 51871092, 51625404, 51771232, and 51671217), State Key Laboratory of Advanced Design and Manufacturing for Vehicle Body (71865015), the Fundamental Research Funds for the Central Universities (531107051151), and the National Key Research and Development Program of China (2016YFB0700300). PKL would like to acknowledge the Department of Energy (DOE), Office of Fossil energy, National Energy Technology Laboratory (DE-FE-0011194) with the program manager, Dr. J. Mullen. PKL very much appreciates the support of the U.S. Army Research Office project (W911NF-13-1-0438 and W911NF-19-2-0049) with the program managers, Dr. M.P. Bakas, Dr. D.M. Stepp, and Dr. S.N. Mathaudhu. PKL thanks the support the National Science Foundation (DMR-1611180 and 1809640) with the program directors, Drs. J. Yang, Drs G. Shiflet and D. Farkas. The authors are thankful for the computational resource provided by the TianHe-1 supercomputer at the National Supercomputer Center in Changsha, China.

Appendix A. Supplementary data

Supplementary data to this article can be found online at https://doi.org/10.1016/j.ijplas.2020.102819.

References

Antillon, E., Woodward, C., Rao, S.I., Akdim, B., Parthasarathy, T.A., 2019. A molecular dynamics technique for determining energy landscapes as a dislocation percolates through a field of solutes. Acta Mater. 166, 658.
Bacon, D.J., Osetsky, Y.N., Rodney, D., 2009. Dislocation–obstacle interactions at the atomic level. Dislocations Solids 15, 1–90.
Bacon, D.J., Kocks, U.F., Scattergood, R.O., 1973. The effect of dislocation self-interaction on the Orowan stress. Philos. Mag. A 8, 1241.
Brown, L.M., Ham, R.K., 1971. Dislocation-particle Interactions. John Wiley and Sons, New York, NY.
Bahramyan, M., Mousavian, R.T., Brabazon, D., 2020. Study of the plastic deformation mechanism of TRIP-TWIP high entropy alloys at the atomic level. Int. J. Plast. 127, 102649.
Chen, G., Peng, Y.G., Zheng, Z., Qi Wang, M., Yu, H., Liu, C.T., 2016. Polysynthetic twinned TiAl single crystals for high-temperature applications. Nat. Mater. 15, 876.
Diao, H.Y., Feng, R., Dahmen, K.A., Liaw, P.K., 2017. Fundamental deformation behavior in high-entropy alloys: an overview. Curr. Opin. Solid State Mater. Sci. 21, 252–266.
Ding, J., Yu, Q., Asta, M., Ritchie, R.O., 2018a. Tunable stacking fault energies by tailoring local chemical order in CrCoNi medium-entropy alloys. Proc. Nat. Acad. Sci. 115, 8919–8924.
Ding, Z.Y., He, Q.F., Wang, Q., Yang, Y., 2018b. Superb strength and high plasticity in laves phase rich eutectic medium-entropy-alloy nanocomposites. Int. J. Plast. 106, 57–72.
Ding, Q., Zhang, Y., Chen, X., Fu, X., Chen, D., Chen, S.J., Gu, L., Wei, F., Bei, H.B., Gao, Y.F., Wen, M.R., Li, J.X., Zhang, Z., Zhu, T., Ritchie, R.O., Yu, Q., 2019. Tuning element distribution, structure and properties by composition in high-entropy alloys. Nature 574 (7777), 223–227.
Esteban-Manzanares, G., Martínez, E., Segurado, J., Capolungo, L., LLorca, J., 2019a. An atomistic investigation of the interaction of dislocations with Guinier-Preston zones in Al-Cu alloys. Acta Mater. 162, 189–201.
Esteban-Manzanares, G., Bellón, B., Martínez, E., Papadimitriou, I., LLorca, J., 2019b. Strengthening of Al–Cu alloys by Guinier–Preston zones: predictions from atomistic simulations. J. Mech. Phys. Solid. 132, 103675.
Fang, Q.H., Li, L., Li, J., Wu, H.Y., Huang, Z.W., Liu, B., Liu, Y., Liaw, P.K., 2019. A statistical theory of probability-dependent precipitation strengthening in metals and alloys. J. Mech. Phys. Solid. 122, 177–189.
Frank, M., Chen, Y., Nene, S.S., Sinha, S., Liu, K., An, K., Mishra, R.S., 2020. Investigating the deformation mechanisms of a highly metastable high entropy alloy using in-situ neutron diffraction. Mater. Tod. Commun. 23, 100858.
Feng, X.B., Zhang, J.Y., Wang, Y.Q., Hou, Z.Q., Wu, K., Liu, G., Sun, J., 2017. Size effects on the mechanical properties of nanocrystalline NbMoTaW refractory high entropy alloy thin films. Int. J. Plast. 95, 264–277.
Foiles, S.M., Baskes, M.I., Daw, M.S., 1986. Embedded-atom-method functions for the fcc metals Cu, Ag, Au, Ni, Pd, Pt, and their alloys. Phys. Rev. B 33, 7983.
Fu, Z., Chen, W., Wen, H., Zhang, D., Chen, Z., Zheng, B., Lavernia, E.J., 2016. Microstructure and strengthening mechanisms in an FCC structured single-phase nanocrystalline Co25Ni25Fe25Al7.5Cu17.5 high-entropy alloy. Acta Mater. 107, 59–71.
Fu, Z., Jiang, L., Wardini, J.L., MacDonald, B.E., Wen, H., Xiong, W., Zhang, D.L., Zhou, Y.Z., Rupert, T.J., Chen, W.P., Lavernia, E.J., 2018. A high-entropy alloy with hierarchical precipitates and ultrahigh strength. Sci. Adv. 4, 8712.
Gao, M.C., Yeh, J.W., Liaw, P.K., Zhang, Y., 2016. High-entropy Alloys. Springer International Publishing.
Ghosh, S.K., Bandyopadhyay, P.S., Kundu, S., Chatterjee, S., 2011. Copper bearing microalloyed ultrahigh strength steel on a pilot scale: microstructure and properties. Mater. Sci. Eng. A 528, 7887–7894.

Gludovatz, B., Hohenwarter, A., Catoor, D., Chang, E.H., George, E.P., Ritchie, R.O., 2014. A fracture-resistant high-entropy alloy for cryogenic applications. Science 345, 1153–1158.
Gludovatz, B., Hohenwarter, A., Thurston, K.V., Bei, H., Wu, Z., George, E.P., Ritchie, R.O., 2016. Exceptional damage-tolerance of a medium-entropy alloy CrCoNi at cryogenic temperatures. Nat. Commun. 7, 10602.
Gwalani, B., Soni, V., Choudhuri, D., Lee, M., Hwang, J.Y., Nam, S.J., Banerjee, R., 2016. Stability of ordered L12 and B2 precipitates in face centered cubic based high entropy alloys-Al0.3CoFeCrNi and Al0.3CuFeCrNi2. Scripta Mater. 123, 130–134.
He, J.Y., Wang, H., Huang, H.L., Xu, X.D., Chen, M.W., Wu, Y., Lu, Z.P., 2016. A precipitation-hardened high-entropy alloy with outstanding tensile properties. Acta Mater. 102, 187–196.
Hirth, J.P., Lothe, J., 1982. Theory of Dislocations. John Wiley, New York.
Huang, H., Wu, Y., He, J., Wang, H., Liu, X., An, K., Lu, Z.P., 2017. Phase-transformation ductilization of brittle high-entropy alloys via metastability engineering. Adv. Mater. 29, 1701678.
Huang, S., Li, W., Lu, S., Tian, F., Shen, J., Holmström, E., Vitos, L., 2015. Temperature dependent stacking fault energy of FeCrCoNiMn high entropy alloy. Scripta Mater. 108, 44–47.
Huang, S., Huang, H., Li, W., Kim, D., Lu, S., Li, X., Vitos, L., 2018a. Twinning in metastable high-entropy alloys. Nat. Commun. 9, 2381.
Huang, H., Li, X., Dong, Z., Li, W., Huang, S., Meng, D., Vitos, L., 2018b. Critical stress for twinning nucleation in CrCoNi-based medium and high entropy alloys. Acta Mater. 149, 388–396.
Ikeda, Y., Körmann, F., Tanaka, I., Neugebauer, J., 2018. Impact of chemical fluctuations on stacking fault energies of CrCoNi and CrMnFeCoNi high entropy alloys from first principles. Entropy 20, 655.
Iskandarov, A.M., Dmitriev, S.V., Umeno, Y., 2011. Temperature effect on ideal shear strength of Al and Cu. Phys. Rev. B 84, 224118.
Jiang, S., Zhang, Y., Wang, S., Zhao, C., 2017a. Plastic deformation mechanisms of equiatomic Ni20Ti20Fe20Al20Cu20 high-entropy alloy at high temperatures. J. Mater. Sci. 52, 3199–3207.
Jiang, S., Wang, H., Wu, Y., Liu, X., Chen, H., Yao, M., Gault, B., Ponge, D., Raabe, D., Hirata, A., Chen, M.W., Wang, Y.D., Lu, Z.P., 2017b. Ultrastrong steel via minimal lattice misfit and high-density nanoprecipitation. Nature 544, 460.
Kirkpatrick, S., Gelatt, C.D., Vecchi Jr., M.P., 1983. Optimization by simulated annealing. Science 220, 671–680.
Kotrechko, S., Dubinko, V., Stetsenko, N., Terentyev, D., He, X., Sorokin, M.J., 2015. Temperature dependence of irradiation hardening due to dislocation loops and precipitates in RPV steels and model alloys. J. Nucl. Mater. 464, 6.
Kuronen, A., Granroth, S., Heinonen, M.H., Perälä, R.E., Kilpi, T., Laukkanen, P., Ropo, M., 2015. Segregation, precipitation, and α− α′ phase separation in Fe-Cr alloys. Phys. Rev. B 92, 214113.
Liang, Y.J., Wang, L., Wen, Y., Cheng, B., Wu, Q., Cao, T., Xiao, Q., Xue, Y., Sha, G., Wang, Y.D., Ren, Y., Li, X.Y., Wang, L., Wang, F., Cai, H.N., 2018. High-content ductile coherent precipitates achieve ultrastrong high-entropy alloys. Nat. Commun. 9, 4063.
Li, J., Fang, Q., Liu, B., Liu, Y., 2018. Transformation induced softening and plasticity in high entropy alloys. Acta Mater. 147, 35.
Li, Y.Z., Huang, M.X., 2018. Revealing the interfacial plasticity and shear strength of a TiB2-strengthened high-modulus low-density steel. J. Mech. Phys. Solid. 121, 313–327.
Li, Q.J., Sheng, H., Ma, E., 2019. Strengthening in multi-principal element alloys with local-chemical-order roughened dislocation pathways. Nat. Commun. 10, 3563.
Lin, C.M., Tsai, H.L., 2011. Evolution of microstructure, hardness, and corrosion properties of high-entropy Al0.5CoCrFeNi alloy. Intermetallics 19, 288–294.
Lei, Z., Liu, X., Wu, Y., Wang, H., Jiang, S., Wang, S., Hui, X., Wu, Y., Gault, B., Kontis, P., Raabe, D., Gu, L., Zhang, Q., Chen, H., Wang, H., Liu, J., An, K., Zeng, Q., Nieh, T., Lu, Z., 2018. Enhanced strength and ductility in a high-entropy alloy via ordered oxygen complexes. Nature 563, 546.
Ma, Y., Jiang, B., Li, C., Wang, Q., Dong, C., Liaw, P.K., Sun, L., 2017. The BCC/B2 morphologies in AlxNiCoFeCr high-entropy alloys. Metals 7, 57.
Middleburgh, S.C., King, D.M., Lumpkin, G.R., Cortie, M., Edwards, L., 2014. Segregation and migration of species in the CrCoFeNi high entropy alloy. J. Alloys Compd. 599, 179–182.
Miracle, D.B., Senkov, O.N., 2017. A critical review of high entropy alloys and related concepts. Acta Mater. 122, 448–511.
Mishin, Y., 2004. Atomistic modeling of the γ and γ′-phases of the Ni–Al system. Acta Mater. 52, 1451.
Ming, K., Bi, X., Wang, J., 2018. Realizing strength-ductility combination of coarse-grained Al0.2Co1.5CrFeNi1.5Ti0.3 alloy via nano-sized, coherent precipitates. Int. J. Plast. 100, 177–191.
Ming, K., Bi, X., Wang, J., 2019. Strength and ductility of CrFeCoNiMo alloy with hierarchical microstructures. Int. J. Plast. 113, 255–268.
Nöhring, W.G., Curtin, W.A., 2017. Dislocation cross-slip in fcc solid solution alloys. Acta Mater. 128, 135.
Osetsky, Y.N., Pharr, G.M., Morris, J.R., 2019. Two modes of screw dislocation glide in fcc single-phase concentrated alloys. Acta Mater. 164, 741.
Onat, B., Durukanoğlu, S., 2013. An optimized interatomic potential for Cu–Ni alloys with the embedded-atom method. J. Phys. 26 (3), 035404.
Plimpton, S., 1995. Fast parallel algorithms for short-range molecular dynamics. J. Comp. Phys. 117, 1.
Praveen, S., Murty, B.S., Kottada, R.S., 2012. Alloying behavior in multi-component AlCoCrCuFe and NiCoCrCuFe high entropy alloys. Mater. Sci. Eng. A 534, 83–89.
Poschmann, M., Lin, J., Geerlings, H., Winter, I.S., Chrzan, D.C., 2018. Strain-induced variant selection in heterogeneous nucleation of α-Ti at screw dislocations in β-Ti. Phys. Rev. Mater. 2, 083606.
Rao, S.I., Varvenne, C., Woodward, C., Parthasarathy, T.A., Miracle, D., Senkov, O.N., Curtin, W.A., 2017a. Atomistic simulations of dislocations in a model BCC multicomponent concentrated solid solution alloy. Acta Mater. 125, 311–320.
Rao, S.I., Woodward, C., Parthasarathy, T.A., Senkov, O., 2017b. Atomistic simulations of dislocation behavior in a model FCC multicomponent concentrated solid solution alloy. Acta Mater. 134, 188–194.
Santos-Güemes, R., Esteban-Manzanares, G., Papadimitriou, I., Segurado, J., Capolungo, L., LLorca, J., 2018. Discrete dislocation dynamics simulations of dislocation-θ′ precipitate interaction in Al-Cu alloys. J. Mech. Phys. Solid. 118, 228–244.
Santodonato, L.J., Zhang, Y., Feygenson, M., Parish, C.M., Gao, M.C., Weber, R.J., Liaw, P.K., 2015. Deviation from high-entropy configurations in the atomic distributions of a multi-principal-element alloy. Nat. Commun. 6, 5964.
Senkov, O.N., Senkova, S.V., Woodward, C., 2014. Effect of aluminum on the microstructure and properties of two refractory high-entropy alloys. Acta Mater. 68, 214–228.
Singh, C.V., Warner, D.H., 2010. Mechanisms of Guinier–Preston zone hardening in the athermal limit. Acta Mater. 58, 5797.
Singh, C.V., Mateos, A.J., Warner, D.H., 2011a. Atomistic simulations of dislocation–precipitate interactions emphasize importance of cross-slip. Scripta Mater. 64, 398–401.
Singh, S., Wanderka, N., Murty, B.S., Glatzel, U., Banhart, J., 2011b. Decomposition in multi-component AlCoCrCuFeNi high-entropy alloy. Acta Mater. 59, 182–190.
Shin, D., Shyam, A., Lee, S., Yamamoto, Y., Haynes, J.A., 2017. Solute segregation at the Al/θ′-Al2Cu interface in Al-Cu alloys. Acta Mater. 327–340.
Smith, T.M., Esser, B.D., Antolin, N., Carlsson, A., Williams, R.E.A., Wessman, A., Mills, M.J., 2016. Phase transformation strengthening of high-temperature superalloys. Nat. Commun. 7, 13434.
Stukowski, A., 2009. Visualization and analysis of atomistic simulation data with OVITO–the Open Visualization Tool. Model. Simulat. Mater. Sci. Eng. 18, 015012.
Stukowski, A., Bulatov, V.V., Arsenlis, A., 2012. Automated identification and indexing of dislocations in crystal interfaces. Model. Simulat. Mater. Sci. Eng. 20, 085007.
Suzuki, H., 1952. Chemical interaction of solute atoms with dislocations. Sci. Rep. Res. Inst. Tohoku Univ. Phys. Chem. Metall. 4, 455.
Sun, X., Zhang, H., Li, W., Ding, X., Wang, Y., Vitos, L., 2020. Generalized stacking fault energy of Al-doped CrMnFeCoNi high-entropy alloy. Nanomaterials 10, 59.
Utt, D., Stukowski, A., Albe, K., 2020. Grain boundary structure and mobility in high-entropy alloys: a comparative molecular dynamics study on a Σ11 symmetrical tilt grain boundary in face-centered cubic CuNiCoFe. Acta Mater. 186, 11–19.
Varvenne, C., Luque, A., Curtin, W.A., 2016. Theory of strengthening in fcc high entropy alloys. Acta Mater. 118, 164–176.
Vikram, R.J., Gaddam, S., Kalsar, R., Acharya, S., Suwas, S., 2019. A fractal approach to predict the oxidation and corrosion behavior of a grain boundary engineered low SFE high entropy alloy. Mater 7, 100398.

Wang, Y.M., Cheng, S., Wei, Q., Ma, E., Nieh, T.G., Hamza, A.V., 2004. Effects of annealing and impurities on tensile properties of electrodeposited nanocrystalline Ni. Scripta Mater. 51, 1023–1028.
Wang, Q., Ma, Y., Jiang, B., Li, X., Shi, Y., Dong, C., Liaw, P.K., 2016. A cuboidal B2 nanoprecipitation-enhanced body-centered-cubic alloy Al0.7CoCrFe2Ni with prominent tensile properties. Scripta Mater. 120, 85–89.
Wang, Y.P., Li, B.S., Fu, H.Z., 2009. Solid solution or intermetallics in a high-entropy alloy. Adv. Eng. Mater. 11, 641.
Wu, S.W., Wang, G., Wang, Q., Jia, Y.D., Yi, J., Zhai, Q.J., Liu, J.B., Sun, B.A., Chu, H.J., Shen, J., Liaw, P.K., Liu, C.T., Zhang, T.Y., 2019. Enhancement of strength-ductility trade-off in a high-entropy alloy through a heterogeneous structure. Acta Mater. 165, 444–458.
Xu, X.D., Liu, P., Guo, S., Hirata, A., Fujita, T., Nieh, T.G., Chen, M.W., 2015. Nanoscale phase separation in a fcc-based CoCrCuFeNiAl0.5 high-entropy alloy. Acta Mater. 4, 145–152.
Yang, Z., Zhang, L., Chisholm, M.F., Zhou, X., Ye, H., Pennycook, S.J., 2018a. Precipitation of binary quasicrystals along dislocations. Nat. Commun. 9, 809.
Yang, T., Zhao, Y.L., Tong, Y., Jiao, Z.B., Wei, J., Cai, J.X., Han, X.D., Chen, D., Hu, A., Kai, J.J., Lu, K., Liu, Y., Liu, C.T., 2018b. Multicomponent intermetallic nanoparticles and superb mechanical behaviors of complex alloys. Science 362, 933–937.
Yao, Y., Huang, Z., Xie, P., Lacey, S.D., Jacob, R.J., Xie, H., Yu, D., 2018. Carbothermal shock synthesis of high-entropy-alloy nanoparticles. Science 359, 1489–1494.
Yin, B.L., Shuhei Yoshida, S., Nobuhiro Tsuji, N., Curtin, W.A., 2020. Yield strength and misfit volumes of NiCoCr and implications for short-range-order. Nat. Commun. 11, 2507.
Yeh, J.W., Chen, S.K., Lin, S.J., Gan, J.Y., Chin, T.S., Shun, T.T., Chang, S.Y., 2004. Nanostructured high-entropy alloys with multiple principal elements: novel alloy design concepts and outcomes. Adv. Eng. Mater. 6, 299–303.
Zaddach, A.J., Niu, C., Koch, C.C., Irving, D.L., 2013. Mechanical properties and stacking fault energies of NiFeCrCoMn high-entropy alloy. JOM 65 (12), 1780–1789.
Zhang, Y., Zhou, Y.J., Lin, J.P., Chen, G.L., Liaw, P.K., 2008. Solid-solution phase formation rules for multi-component alloys. Adv. Eng. Mater. 10, 534–538.
Zhang, Y., Zuo, T.T., Tang, Z., Gao, M.C., Dahmen, K.A., Liaw, P.K., Lu, Z.P., 2014. Microstructures and properties of high-entropy alloys. Prog. Mater. Sci. 61, 1–93.
Zhang, Y., Stocks, G.M., Jin, K., Lu, C., Bei, H., Sales, B.C., Caro, M., 2015. Influence of chemical disorder on energy dissipation and defect evolution in concentrated solid solution alloys. Nat. Commun. 6, 8736.
Zhang, X., Yao, J., Liu, B., Yan, J., Lu, L., Li, Y., Gao, H.J., Li, X., 2018a. Three-dimensional high-entropy alloy–polymer composite nanolattices that overcome the strength–recoverability trade-off. Nano Lett. 18, 4247–4256.
Zhang, L., Zhou, Y., Jin, X., Du, X., Li, B., 2018b. Precipitation-hardened high entropy alloys with excellent tensile properties. Mater. Sci. Eng. A 732, 186–191.
Zhang, Z., Sheng, H., Wang, Z., Gludovatz, B., Zhang, Z., George, E.P., Ritchie, R.O., 2017. Dislocation mechanisms and 3D twin architectures generate exceptional strength-ductility-toughness combination in CrCoNi medium-entropy alloy. Nat. Commun. 8, 14390.
Zhang, R., Zhao, S., Ding, J., Chong, Y., Jia, T., Ophus, C., Colin, O., Mark, A., Robert, O.R., Minor, A.M., 2020. Short-range order and its impact on the properties of the CrCoNi medium entropy alloy. Nature 581, 283.
Zhao, S., Osetsky, Y., Stocks, G.M., Zhang, Y., 2019. Local-environment dependence of stacking fault energies in concentrated solid-solution alloys. npj Comp. Mater. 5, 13.
Zhao, Y.Y., Chen, H.W., Lu, Z.P., Nieh, T.G., 2018. Thermal stability and coarsening of coherent particles in a precipitation-hardened $(NiCoFeCr)_{94}Ti_{2}Al_{4}$ high-entropy alloy. Acta Mater. 147, 184–194.
Zhou, X., Li, X.Y., Lu, K., 2018. Enhanced thermal stability of nanograined metals below a critical grain size. Science 360, 526–530.
Zhou, N., Shen, C., Mills, M.J., Li, J., Wang, Y.Z., 2011. Modeling displacive–diffusional coupled dislocation shearing of γ′ precipitates in Ni-base superalloys. Acta Mater. 59, 3484.
Zhou, X.W., Johnson, R.A., Wadley, H.N.G., 2004. Misfit-energy-increasing dislocations in vapor-deposited CoFe/NiFe multilayers. Phys. Rev. B 69, 144113.
Zhuang, Y.X., Xue, H.D., Chen, Z.Y., Hu, Z.Y., He, J.C., 2013. Effect of annealing treatment on microstructures and mechanical properties of FeCoNiCuAl high entropy alloys. Mater. Sci. Eng. A 572, 30.
Zou, Y., Ma, H., Spolenak, R., 2015. Ultrastrong ductile and stable high-entropy alloys at small scales. Nat. Commun. 6, 7748.